

TANTALUM CLUSTERING IN THE A1 TO L1₀ IRON-PLATINUM-TANTALUM
CHEMICAL ORDERING PHASE TRANSFORMATION

By

DIONDRA MEANS

A THESIS

Submitted in partial fulfillment of the requirements
for the degree of Master of Science
in the Department of Metallurgical and Materials Engineering
in the Graduate School of
The University of Alabama

TUSCALOOSA, ALABAMA

2010

Copyright Diondra Means 2010
ALL RIGHTS RESERVED

ABSTRACT

A series of $\text{Fe}_{52}\text{Pt}_{48}$, $\text{Fe}_{52.3}\text{Pt}_{46.3}\text{Ta}_{1.4}$ and $\text{Fe}_{52}\text{Pt}_{40.7}\text{Ta}_{7.3}$ thin films were sputter-deposited and subsequently annealed at 550°C and 750°C for 30 min. The as-deposited films adopted the A1 phase. The addition of Ta resulted in the change in the $\{111\}$ to $\{200\}$ fiber texture for these films. This has been explained in terms of the competition between surface energy and strain energy. The $\text{Fe}_{52}\text{Pt}_{48}$ and $\text{Fe}_{52.3}\text{Pt}_{46.3}\text{Ta}_{1.4}$ films ordered into $L1_0$ at 550°C but the $\text{Fe}_{52}\text{Pt}_{40.7}\text{Ta}_{7.3}$ did not. Upon annealing at 750°C all three films phase transformed to the $L1_0$ phase. As the Ta concentration increased, the grain size was refined and hindered grain growth. Atom probe tomography revealed nano-scale clustering upon annealing for films that contained Ta. For the lower 1.4 at. % Ta concentration film, these clusters were predominately within the grains. For the 7.3 at. % Ta film, the clusters formed predominately in the grain boundaries. The formation of clusters appears to be a necessary initial step to allow the short range A1 to $L1_0$ ordering processes in FePt to occur.

DEDICATION

I dedicate this thesis to my Lord savior above, to whom I am nothing without. This road would have been a whole lot bumpier without Him. Also to everyone who has aided me in writing this manuscript.

LIST OF ABBREVIATIONS AND SYMBOLS

<i>FIB</i>	Focused ion beam
<i>TEM</i>	Transmission electron microscopy
<i>SEM</i>	Scanning electron microscopy
<i>XRD</i>	X-ray diffraction
<i>LEAP</i>	Local electrode atom probe
<i>APT</i>	Atom probe tomography
<i>AGM</i>	Areal gradient magnetism
<i>DF</i>	Dark field image
<i>S</i>	Order parameter
<i>°C</i>	Degree Celsius
<i>H_c</i>	Coercivity
<i>A1</i>	FePt disordered FCC phase
<i>L1₀</i>	FePt ordered FCT phase
<i>μm</i>	micron
<i>λ</i>	Wavelength
<i>mA</i>	Milliamp
<i>kV</i>	Kilovolts
<i>μ</i>	mu (magnitude of random deviation)

ACKNOWLEDGMENTS

I am sincerely grateful to have a research and academic advisor who also served as my mentor. Thank you, Dr. Greg Thompson for your continued emotional support and academic guidance with the completion of this work. I would also like to thank all of my group members who helped me along the way. With a special thanks to Karen Torres, Robert Morris, Bianzhu Fu, and Billie Wang. I gratefully appreciate the time and effort given to me to help with the completion of this manuscript. Thanks to the CAF for providing me with the access to research equipment and the CAF staff: Rich Martens, Johnny Goodwin, and Rob Holler; I am indebted to you.

I would also like to thank Professors Mark Weaver and Oleg Mryasov for serving on my committee. I appreciate the suggestions provided, as this will help me become more thorough in my research career.

To my family and friends, who relentlessly supported and encouraged me during my pursuit for an advanced degree. Also, I would like to acknowledge my fiancé Lu, thank you my love for helping me stay focused.

This work was supported by the Louis Stokes Award for Minority Participation Fellowship and the National Science Foundation Grant DMR-0529369.

CONTENTS

ABSTRACT.....	ii
DEDICATION.....	iii
LIST OF ABBREVIATIONS AND SYMBOLS	iv
ACKNOWLEDGMENTS	v
LIST OF TABLES.....	viii
LIST OF FIGURES	ix
1. INTRODUCTION	1
2. EXPERIMENTAL PROCEDURES.....	8
2.1. MAGNETRON SPUTTERING.....	8
2.2. ANNEALING TREATMENTS.....	11
2.3. X-RAY DIFFRACTION (XRD).....	12
2.4. MAGNETOMETRY.....	12
2.5. TRANSMISSION ELECTRON MICROSCOPY (TEM).....	14
2.6. ATOM PROBE TOMOGRAPHY (APT)	16
2.6.1. LIFT-OUT PROCEDURE.....	17
2.6.2. ATOM PROBE DATA ANALYSIS	22
3. RESULTS AND DISCUSSION.....	25
3.1. X-RAY DIFFRACTION (XRD)	25
3.2. MAGNETOMETRY.....	27

3.3. GRAIN GROWTH	30
3.4. ATOM PROBE RESULTS	30
4. CONCLUSION AND FUTURE WORK	49
REFERENCES	52
APPENDIX.....	55
A. GRAIN SIZE HISTOGRAMS.....	55
B. SOULTE ANALYSIS PARAMETERS AND PROCEDURES.....	58

LIST OF TABLES

Table 1.1 Summary of reference studies.....	6
Table 3.1 Cluster data for $\text{Fe}_{52.3}\text{Pt}_{46.3}\text{Ta}_{1.4}$ annealed at 550°C	36
Table 3.2 Cluster data for $\text{Fe}_{52}\text{Pt}_{40.7}\text{Ta}_{7.3}$ annealed at 550°C	36
Table 3.3 Cluster data for $\text{Fe}_{52.3}\text{Pt}_{46.3}\text{Ta}_{1.4}$ annealed at 750°C	44
Table 3.4 Cluster data for $\text{Fe}_{52}\text{Pt}_{40.7}\text{Ta}_{7.3}$ annealed at 750°C	47
Table B.1 Mu (μ) values from statistical analysis	58
Table B.2 IVAS 3.4.1 input parameters for identification of clusters	58

LIST OF FIGURES

1.1 A1 to L1o phase transformation model	3
1.2 Grain size values and trends taken from reference papers.....	7
2.1 Photograph of AJA sputtering chamber.....	9
2.2 Film growth sequence	10
2.3 Goniometer configuration.....	13
2.4 TEM image of grains	15
2.5 Preparation of atom probe specimen.....	18
2.6 Attachment and sharpening of atom probe sample.....	20
3.1. XRD scans of thin films.....	26
3.2. Order parameter plotted as a function of temperature	28
3.3 Magnetic properties	29
3.4 Plot of grain size as a function of temperature	31
3.5 Statistical clustering data for as-deposited 1.4 at. % Ta film.....	32
3.6 Clustering data for 1.4 at. % Ta film annealed at 550°C	34
3.7 Atom map and clustering data for 7.3 at. % film annealed at 550°C...35	
3.8 Proxigram data of 1.4 at. % Ta film annealed at 550°C	38
3.9 Proxigram data of 1.4 at. % film annealed at 750°C.....	39
3.10 Proxigram data of 7.3 at. % Ta film annealed at 550°C	40

3.11 Proxigram data of 7.3 at. % film annealed at 750°C.....	41
3.12 Clustering data for 1.4 at. % Ta film annealed at 750oC.....	43
3.13 Clustering data for 7.3 at. % film annealed at 750°C.....	45
A.1 Grain size histograms and images for binary FePt film	55
A.2 Grain size histograms and images for 1.4 at. % Ta film	56
A.3 Grain size histograms and images for 7.3 at. % Ta film	57
B.1 Voxel schematic	58
B.2 Screen shot of IVAS solute analysis steps	59

CHAPTER 1

INTRODUCTION

The high magnetocrystalline anisotropy, K_u , of the $L1_0$ FePt phase makes it a leading candidate for ultra-high magnetic storage media applications.¹ Magnetic media comprises of small grains which are magnetically exchanged coupled to each other in groups referred to as bits. As the density increases, the bits, or grain sizes, must decrease. However, reduction of the grain sizes, or volume, will result in the magnetization being subject to random fluctuations because of thermal effects, kT , where k is Boltzmann's constant and T is temperature. This size-temperature dependent switching of magnetization is referred to as the superparamagnetic limit and is a significant challenge to increasing the storage capacity of magnetic media. The magnetization switching is given by the Arrhenius equation,

$$\tau_N = \tau_o \exp\left(\frac{KV}{k_B T}\right) \quad (1.1)$$

where τ_N is the average time between changes in magnetization direction, τ_o is the materials attempt time, V is the volume and the other terms have been defined above. From this equation, the advantage of $L1_0$ FePt is clear. If the volume decreases, as required by increasing the density of bits, the K_u must increase to make the magnetization stable for long term magnetic storage. FePt's K_u is approximately 7×10^7 ergs/cc which can make the magnetization thermally stable for grain sizes approaching approximately 4 nm in diameter.²⁻⁴ To date, the majority of current magnetic media is comprised of CoPtCr alloys with grain sizes of approximately 8-10 nm.⁵

When FePt is deposited as a thin film, it adopts a magnetically soft, solid-solution, face-center-cubic phase denoted as A1 (Fm3m space group). In order to obtain the magnetically hard $L1_0$ phase (P4/mmm space group), an *ex situ* anneal at temperatures > 500 °C is required.⁶⁻⁷ The two crystal structures are shown in figure 1.1. Annealing results in grain coarsening and the loss of the narrow grain size distribution needed for ultra-high magnetic storage media applications. Considerable research has been devoted to understanding how to anneal FePt into $L1_0$ while reducing or eliminate the detrimental grain growth.^{10,11}

The A1 to $L1_0$ FePt phase transformation is a polymorphic reaction, which means a change in crystal structure and no change in composition between the two phases. This would suggest short range diffusion is required rather than long range atomic transport. Also, the reaction is believed to commence by a discontinuous precipitation process.⁷ Discontinuous precipitation occurs by phase transforming a material behind a reaction front usually at a grain boundary. This can lead to abnormal grain growth.^{7,8} The grain boundaries provide sources and sinks for vacancies that can assist in the diffusion ordering process.

There has been significant research interest in the use of ternary alloying additions which could lower the ordering temperature thus reducing the extent of grain growth that occurs at elevated temperatures. In addition, ternary elements that segregate to grain boundaries could control the grain growth by pinning the grain boundaries.⁹ For example; additions such as Ag or Au have been shown to have modest reductions to the FePt ordering temperature while hindering grain growth. The Ag or Au atoms are rejected from the bulk of the grain and migrate to the grain boundaries.^{10,11}

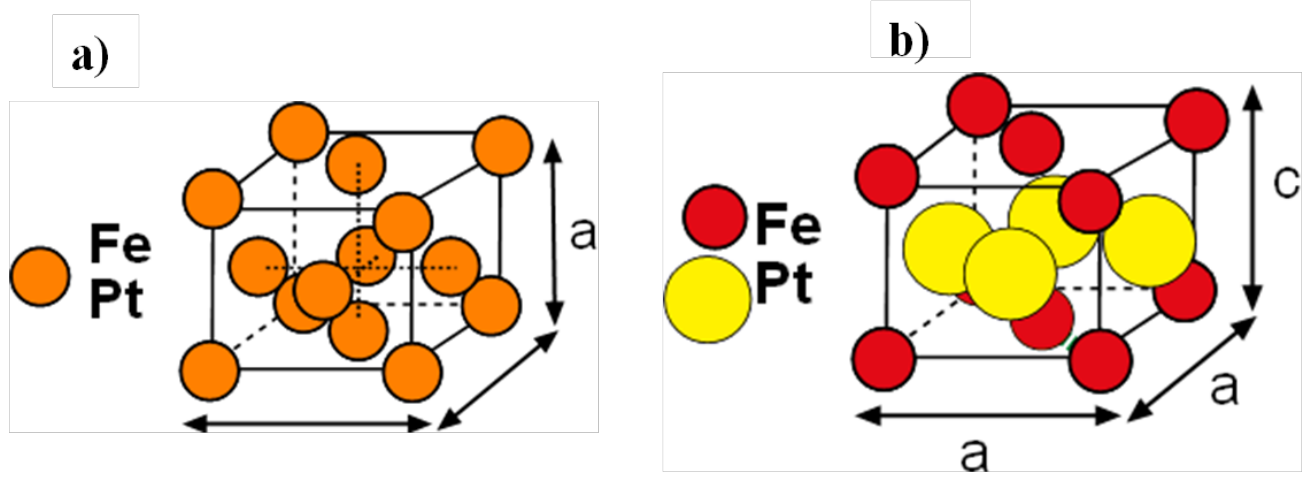


Figure 1.1 Crystal structures of (a) A1 and (b) $L1_0$ FePt.

However, minor additions of Cu have been shown to reduce the ordering temperature but, unfortunately, facilitated grain growth.¹² Other ternary additions like Cr and Zr have resulted in the chemical reactions with the FePt resulting in subsequent deleterious precipitation of other intermetallic phases.¹³⁻¹⁴

Arguably, ternary additions have had mixed success in controlling both the ordering temperature and grain growth. Without a better understanding of how ternary additions effect FePt ordering and microstructure, the full advantage of these alloy additions cannot be achieved or engineered. This thesis aims at providing a detailed microstructural study in how the ternary addition, Ta, effects order and grain growth in FePt.

There have been some conflicting reports on the use of the Ta and how it changes the ordering temperature in FePt. Jin *et al.*¹⁵ reported a decrease in the ordering temperature with Ta additions where as Chu *et al.*¹⁶ reported that Ta increased the ordering temperature as compared to an unalloyed FePt film. Jin *et al.*'s¹⁵ samples were Fe₄₅Pt₅₅ films with Ta additions of 0.2, 1.5, and 5.5 at. %. The films were deposited by three separate elemental targets via DC and RF magnetron sputtering. Jin *et al.*¹⁵ suggested that the ordering process is promoted by the diffusion of Ta from the FePt lattice into the grain boundaries. This is a peculiar result as Pt-rich compositions of FePt are normally considered to require higher temperatures to anneal¹⁸; this result adds more curiosity on how Ta additions could be alternating the phase transformation behavior.

Chu *et al.*'s¹⁷ samples were close to equi-atomic FePt with 3.6, 7.9, and 11.6 at % Ta. These films were deposited by RF magnetron sputtering. Upon heating at 600°C for 1 hour, the 3.6 and 7.9 at. % Ta doped films phase transformed to the ordered L1₀ phase.

The same annealing treatment was applied to the 11.6 at. % Ta film; however, at this concentration, the formation of the ordered phase was inhibited. This indicated that higher concentrations of Ta suppressed ordering. Chu's *et al.*'s¹⁵ hypothesized that this occurred because of the size difference of the Ta atoms with respect to the binary Fe and Pt constituent elements.

Similarly to Chu *et al.*¹⁶, Chen *et al.*¹⁷ reported that ordering commenced at higher temperatures with Ta doping as compared to unalloyed FePt. These samples had a Ta content range from 0 at.% to 2 at. %. They were then annealed between 400°C and 600°C for 100 minutes. Chen *et al.*¹⁷ attributed the impediment to ordering to the segregation of Ta atoms to the grain boundaries, but no direct chemical-microstructural evidence to this assertion was given. Chen *et al.*'s¹⁷ explanation contradicts the mechanism for the lower order given by Jin *et al.*¹⁵, *e.g.* that the Ta migration to the grain boundaries facilitated ordering.

In all three reports¹⁵⁻¹⁷, the grain size, as measured by the Scherrer's formula in the X-ray diffraction spectra, showed a refined grain size for films with Ta. This is believed to be because of the Ta segregation to grain boundaries, yet there is no direct microstructural observation of this segregation. If Ta does segregate, as suspected, it could have the added benefit of reducing the exchange coupling between the grains. The addition of Cr to magnetic films has been known to hinder exchange coupling by segregating to the grain boundaries and refine the grain structure. Unlike Cr¹³, which resulted in deleterious precipitation of other phases with FePt, Ta may not suffer from this issue.

Clearly from the limited number studies of Ta additions, there is a lack of consensus on its effect on the ordering behavior in FePt. A summary of their results are shown in table 1.1. All reports¹⁵⁻¹⁷ suggested that Ta inhibited grain growth. The grain size values and trends are shown in figure 1.2 taken from data given in the referenced papers. The lack of direct microstructural characterization, at the atomic level, hinders the ability to fully rationalize how Ta affected the ordering transformation or inhibited the grain growth. Providing such results of would provide a clearer understanding how ternary alloy additions, in general, can be engineered to achieve an optimal FePt thin film microstructure for ultra-high magnetic storage media. This thesis addresses the ordering transformation and microstructure formations for a series of FePt thin films with various amounts of Ta to elucidate its effect on the microstructural stability in $L1_0$ FePt thin films.

Table 1.1 Summary of reference studies.

	Film Composition	Order Transformation	Grain Size	Coercivity
<i>Jin et al.</i>	$\text{Fe}_{45}\text{Pt}_{55}\text{Ta}_{(0.2,1.5,5.5)}$	promoted	decreased	enhanced
<i>Chen et al.</i>	$(\text{Fe}_{72}\text{Pt}_{28})_{1-x}\text{Ta}_{x=(0-2)}$	suppressed	decreased	decreased
<i>Chu et al.</i>	$(\text{FePt})_{100-x}\text{Ta}_{x=(3,6,7,9,11,6)}$	suppressed only in 11.6 at.% film	decreased	decreased

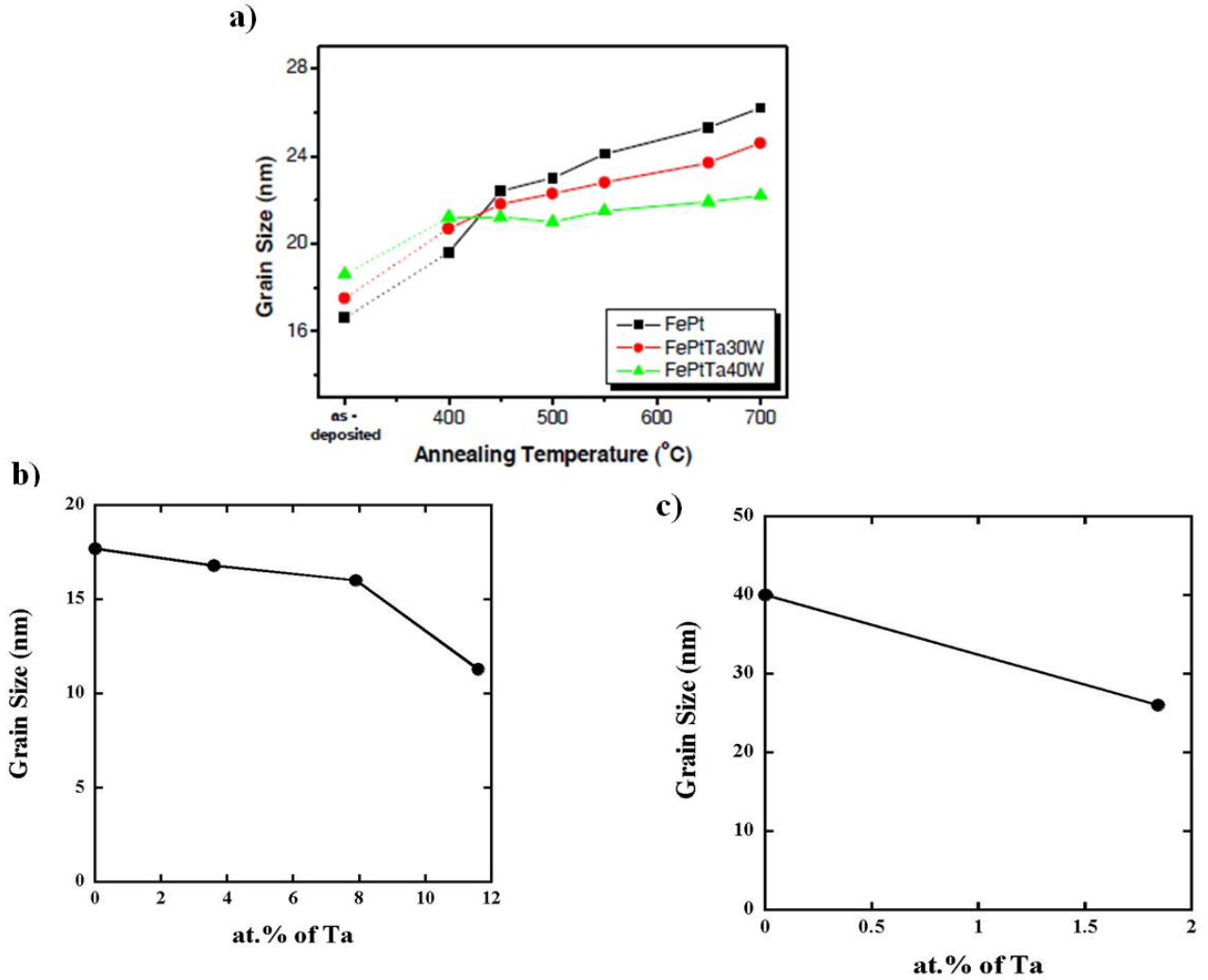


Figure 1.2 (a) Plot taken from Jin *et. al.*'s [15] work. The grain sizes were calculated using the Scherrer equation. The atomic percent of Ta is 1.5 for 30W and 5.5 for 40W. (b) Chu *et. al.*'s [16] grain size values taken from the Scherrer equation. The temperature anneal was at 600°C for 1 hour. (c) Average grain size values taken from Chen *et. al.* [17] depicting the reduction of grain size at the amount of Ta increased. Heat treatments varied from 400°C-600°C for 100 minutes.

CHAPTER 2

EXPERIMENTAL PROCEDURES

2.1 Magnetron Sputtering

Three thin films were direct current (DC) sputter-deposited in an AJA ATC-1500 stainless sputtering unit, shown in figure 2.1. Prior to deposition, the base pressure was $< 3 \times 10^{-7}$ Torr where upon ultra-high purity Ar gas was flowed into the chamber at 10 standard cubic centimeters per minute to a partial pressure of 2 mTorr and served as the sputtering working gas. The three films were $\text{Fe}_{52}\text{Pt}_{48}$, $\text{Fe}_{52.3}\text{Pt}_{46.3}\text{Ta}_{1.4}$ and $\text{Fe}_{52}\text{Pt}_{40.7}\text{Ta}_{7.3}$ and whose composition was controlled by the individual sputtering rates from each target. The compositions of the films were verified by either X-ray energy dispersive spectroscopy (EDS) in a Philips XL30 Scanning Electron Microscope (SEM) operated at 30 keV and/or appropriate ranging from the time-of-flight mass spectrometer in an Imago Scientific Instruments Local Electrode Atom Probe (LEAP®) 3000XSi. The films were grown from elemental Fe, Pt and Ta sputtering targets of commercial purity (> 99.5 at. %). The total film consisted of a stack, repeated four times, of $(\text{Si}_3\text{N}_4)_{10\text{nm}}/(\text{FePtTa}_x)_{30\text{nm}}$ or $(\text{FePt})_{30\text{nm}}/(\text{Si}_3\text{N}_4)_{10\text{nm}}$, shown in figure 2.2.



Figure 2.1 Photograph of sputtering chamber

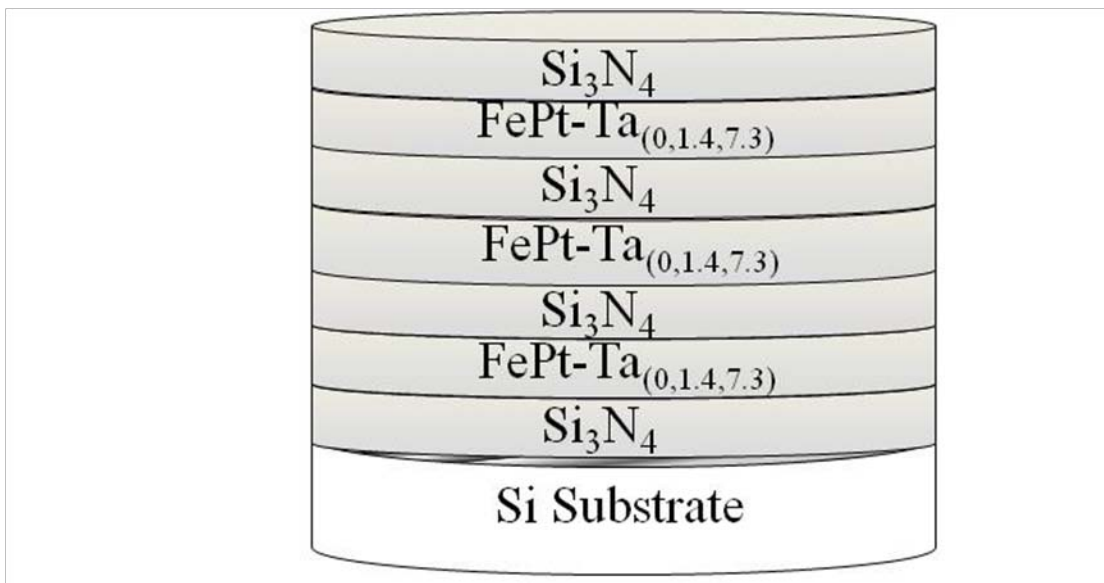


Figure 2.2 Schematic depicting film growth sequence.

The multilayered stack allowed sufficient scattering volume for X-ray intensities to be collected as well as increasing the probability of capturing the region of interest (ROI) when preparing the atom probe tips, described below. The $\text{Fe}_{52}\text{Pt}_{48}$ film provided the base-line comparison to the Ta additions films. The Si_3N_4 under- and over- layers were radio frequency (RF) sputter deposited from a composite target, which provided a barrier layer for the FePt or $\text{Fe}_{52}\text{Pt}_x\text{Ta}_{1-x}$ films from each other within the stack as well as possible oxidation with the atmosphere during the *ex situ* anneals or reactions with the Si substrate.

2.2 Annealing Treatments

Post-deposition the films were diced into 5 mm x 5 mm squares and *ex situ* annealed in a quartz tube that was evacuated and backfilled to 30 Torr with the reducing environment of Ar/4% H_2 . The films were annealed for 30 minutes at 350 °C, 550 °C and 750 °C. The start time for annealing was taken when the sample achieved the desired temperature set point, which was verified by an external thermocouple bonded to the backside of a Si wafer that was placed near the films. Ramp up times depended on the set point, but in general this took between 4 to 10 minutes. Once 30 minutes was over, the samples were retracted from the furnace and allowed to cool, in the backfilled quartz tube, to room temperature, which took approximately 20 minutes.

2.3 X-ray Diffraction (XRD)

The phase and $L1_0$ order parameter, S , were quantified by X-ray diffraction (XRD) using a Bruker Discovery D8 Diffractometer with a CoK_α radiation source ($\lambda=1.789$) operated at 40 keV and 35 mA. The order parameter, S , was calculated using

$$S^2 = \frac{(I_{001}/I_{002})_{exp}}{(I_{001}/I_{002})_{calc}} \quad (2.1)$$

where I_{001}/I_{002} are the integrated intensities for the designated $\{hkl\}$ reflections. The calculated intensity ratio was taken from the JCPDS # 03-065-9121.¹⁸

In general, the as-deposited films exhibited a strong $\{111\}$ fiber texture. To resolve the superlattice reflections, the films were tilted to 35° in χ (chi), which is the angle between the $[111]$ and $[110]$ directions. The tilt angles of the goniometer and sample are shown in figure 2.3(a-b). The integrated intensities were fitted to a Lorentz profile using OriginPro 8 software.

2.4 Magnetometry

The magnetic properties were measured using a Princeton Instruments Model 2900 alternating gradient magnetometer (AGM) with a parallel probe. The AGM has a maximum saturating field of 18 kOe. Data collected during these experiments produced a hysteresis loop showing the relationship between the induced magnetic flux density (B) and the magnetizing force (H). The loop is generated by measuring the magnetic flux of a ferromagnetic material while the magnetizing force is changed. The limited saturation field, for some samples, prevented full saturation and the coercivity, H_c , values reported may be a slight underestimation.

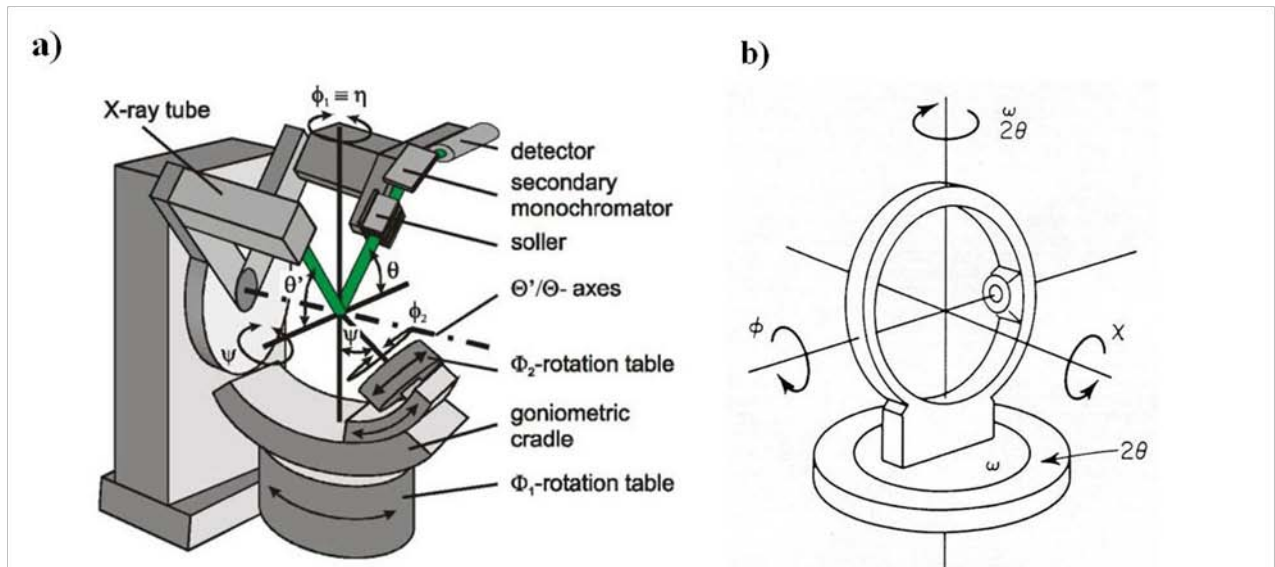


Figure 2.3 (a) Schematic illustrating the basic configuration of a diffractometer taken from <http://www.helmholtz-berlin.de.html>. (b) Sample orientation in diffractometer taken from Scintag Inc.'s XRD manual.

2.5 Transmission Electron Microscopy (TEM)

The microstructure was quantified by Transmission Electron Microscopy (TEM). The TEM foils were prepared by ultrasonic cutting into 3 mm discs, standard backside polishing the Si wafer to $< 100 \mu\text{m}$ and dimpling with diamond paste abrasive to $< 15 \mu\text{m}$. The foil was then milled perforation for electron transparency near the edges of the holes using a Gatan PIPS operated at 3.5 KeV and 20 μA with gun tilt angles of 6° to 8° . The foils were examined in a FEI Tecnai F20 TEM.

The grain size distribution was taken from approximately 50 grains imaged in a dark field (DF) mode using the $\{111\}$ reflection. The grains were manually outlined and measured using the Nikon Elements software platform. Figure 2.4 shows a representative micrograph of how the grains were outlined.

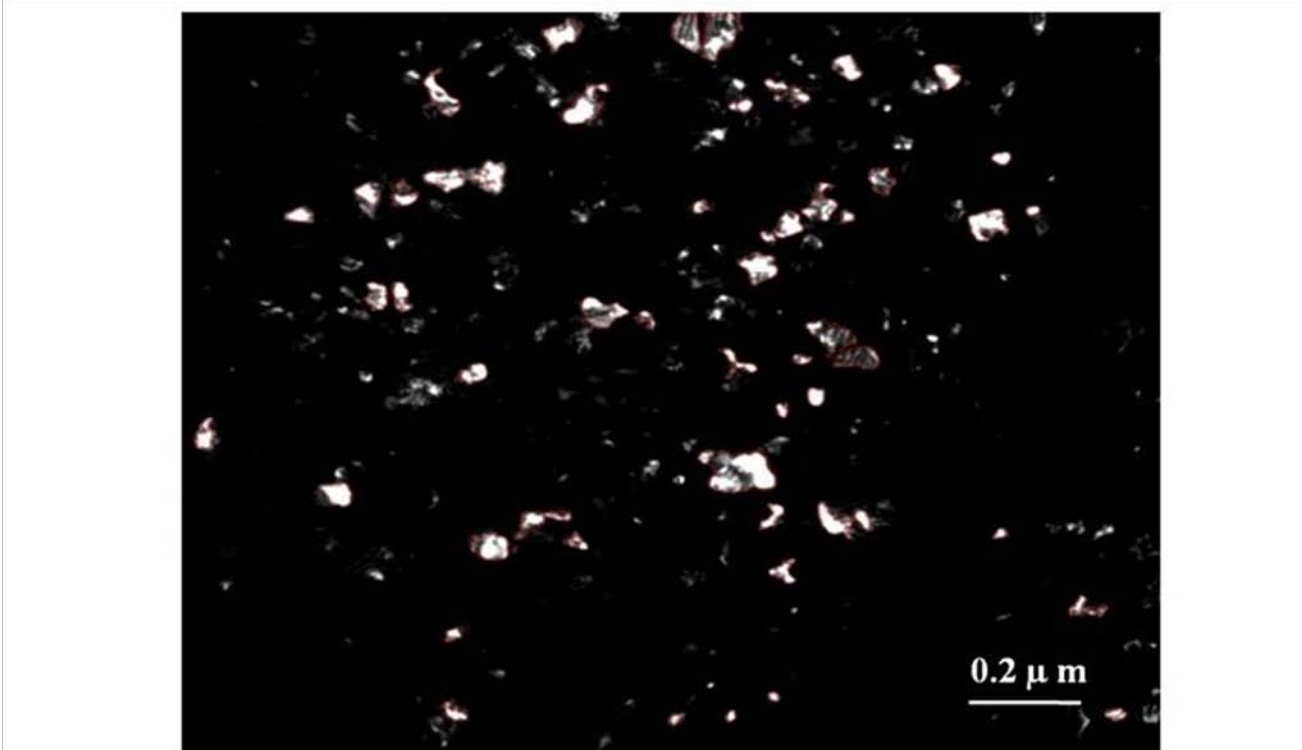


Figure 2.4 TEM micrograph representing grain outline (red) at 9.9 kX magnification.

2.6 Atom Probe Tomography (APT)

In addition to TEM, atom probe tomography (APT) was used to quantify the microstructure. The atom probe instrument field evaporates atoms from a specimen of interest and these atoms (now ions) are collected on a position-sensitive, mass-spectrum detector. By reconstructing the trajectory path and impact position of each ion from the field evaporation event, a volumetric reconstructed rendering of the material is generated with near atomic precision for each individual atom.²⁰ The experiments were conducted in an Imago Scientific Instruments Local Electrode Atom Probe (LEAP®) 3000XSi. The atom probe tips were analyzed the LEAP® in a laser pulsing mode with laser pulse energy of 0.20 - 0.35 nJ at a pulse rate of 250 kHz and at a base temperature of ~ 30 K.

One of the critical requirements for an atom probe specimen is that the ROI is captured into a hemispherical tip with a radius of curvature of approximately 50 to 100 nm. Consequently, a few thousands volts is able to produce a sufficient electric field at the tip to field evaporate the atoms from the surface. In addition to a pulsing the voltage, a standing voltage with a low energy thermal laser pulse can also field evaporate atoms. By pulsing either the voltage or laser, the time-of-flight of each ion is measured and used for reconstructing the z-component in the data spatial positions.

This is used in conjunction with the x-y impact of the ion on the atom probe's microchannel, delay line detector yielding all the data needed for the 3D volume reconstruction of the atoms in the specimen. In addition, the pulsing allows time-of-flight mass spectroscopy for identifying the ion (atom) type.²⁰⁻²²

To sharpen the samples into the appropriate APT specimen geometry, the material is annular ion milled using a FEI Quanta 3D dual electron-focus ion beam (FIB) microscope. The ion beam current was set between 0.3 to 3.0 nA at 30 keV with a final 5 keV ‘clean up’ step to reduce the Ga implantation damage to the surface of the sample. The dual beam FIB’s electron column allows the user to view the sample during milling without damaging the specimen. *In situ* micromanipulation was used to extract a rectangular bar of specimen from the substrate, in a manner described by Thompson *et al.*²² and expanded for thin films by Torres and Thompson.²³ The lift out process for making an atom probe specimen is described in detail below.

2.6.1 Lift-out Procedure

In order to reduce ion beam damage during extraction and obtain a larger ROI, the thin film on the substrate was loaded at 90° to the ion column, as shown in figure 2.4. The defined ROI is protected with an *in situ* deposited strip of Pt. This Pt strip is formed from an organo-metallic gas that is flowed over the surface and breaks down and deposits as a film under the scanned region of the ion beam. The beam was set at 0.3 nA and 30 keV. The dimensions of the Pt strip was about 2 μm wide x 30 μm long x 1 μm thick, figure 2.5 (a)

After the ROI is protected, the milling process begins. A wedge shape region is cut out by titling the sample stage 22° such that the ion beam is no longer normal to the specimen surface. At a scan rotation of 180°, a rectangular cut along the bottom of the Pt bar is done such that the specimen wedge is 2 μm wide x 35 μm long x 5 μm in depth. To reduce the milling time, the current range was between 5-7 nA. The sequence of cuts is shown in figure 2.5 (a-f).

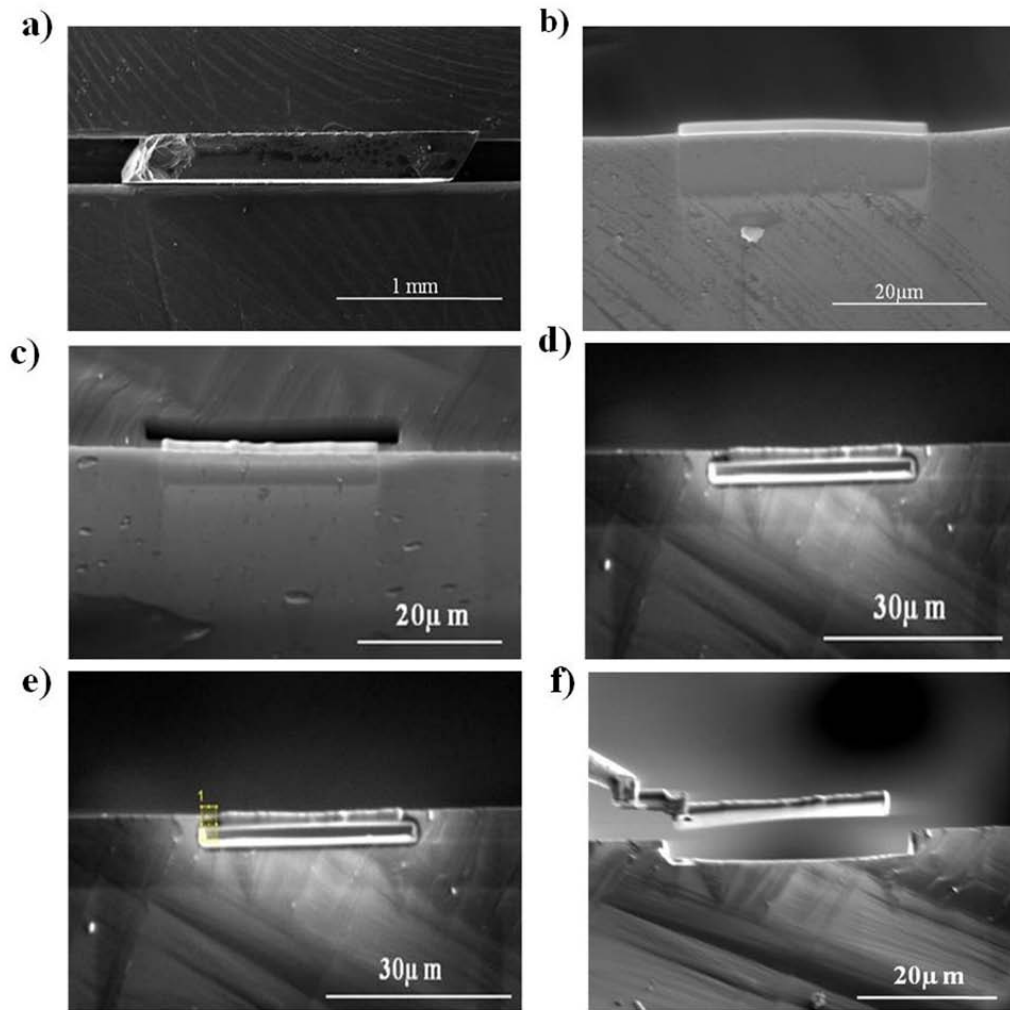


Figure 2.5 Sequence of steps in creating atom probe specimen: (a) The sample is loaded at an angle of 90° , (b) Pt is deposited (c-d) mill through other side of Si wafer, (e) cut releasing wedge from wafer (f) and sample wedge is released from Si wafer.

Once the wedge has been cut, the specimen stage is tilted to 0 ° and a mill cut along the bottom of the wedge is done to release the wedge. The mill cut is made with the ion beam on the left side of the Pt bar. The micromanipulator is then brought in and attached to the end to the wedge with a small *in situ* deposition of Pt. FIB images of the attachment and lift out of wedge are shown in figure 2.5(f)

Once the wedge is detached, it is ready to be connected to a Si microtip array (a Si coupon that includes an array of pre-formed Si posts) for handling. The specimen wedge is then positioned to be on top of the Si post and secured with the *in situ* deposition of Pt.

Once the wedge is secured, using the ion beam the remaining wedge is cut from the mounted sample. The remaining wedge, which is still connected to the *in situ* micromanipulator, is moved to the next post and the process of attachment is repeated.

Once all desired specimens are attached to the Si handling posts, the array of post is rotated 180° and Pt is deposited to fill in the gap created between the tip and sample wedge. Figure 2.6 (a-b) shows micrographs of this procedure.

Once the specimen is attached to the post, it is annular ion milled into a needle shape, shown in figure 2.6 (c). The desirable final tip shape should have a radius of curvature <100 nm. A larger tip radius offers a wider field of view but requires a higher voltage to achieve the evaporation fields which may exceed the specifications of the LEAP ®. To achieve the appropriate tip shape, a series of annular mill patterns are applied. The rough milling is done at 3.0 nA and removes the majority of the sample and forms the general needle shape. The annular pattern has a pre-set inner radius of 3 µm and outer radius of 10 µm or a diameter that is slightly larger than the Si post width.

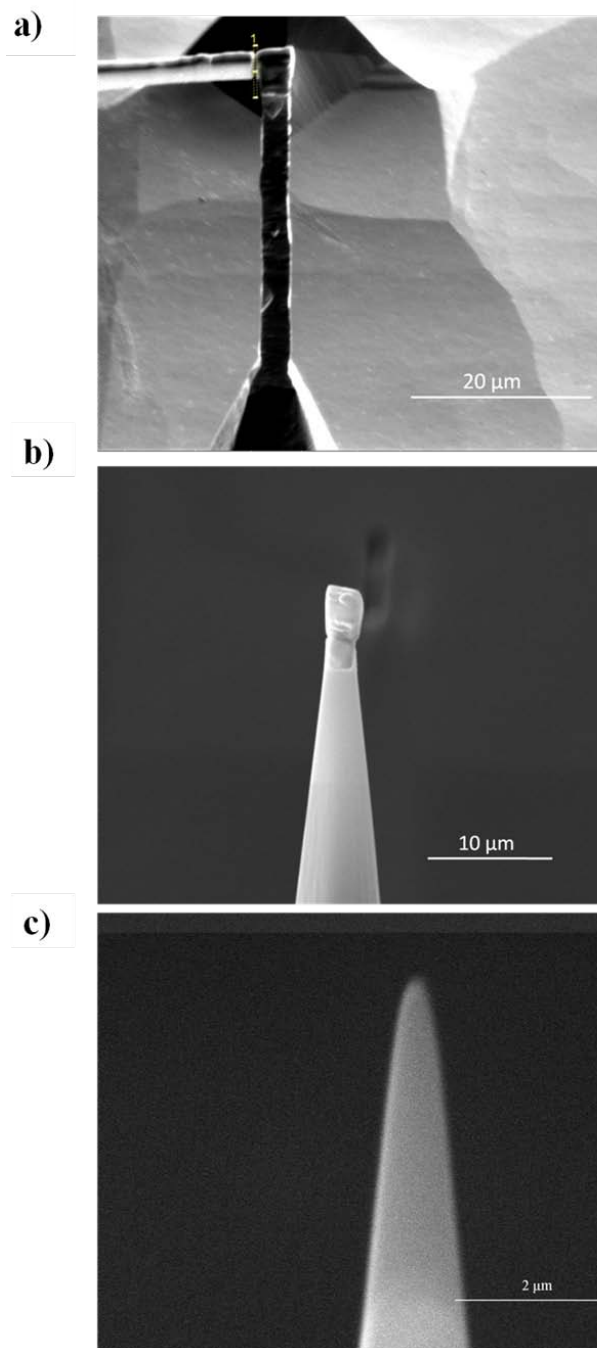


Figure 2.6 Images showing the (a) placement of the wedge on the Si post (b) wedge attachment and (c) final tip shape after sharpening and cleaning steps have been applied.

Only regions between these two diameters are milled. During the course of shaping the needle, the inner radius of the mill pattern is reduced to < 100 nm, which allows the tip of the needle to be milled into shape necessary for the geometric field evaporation requirements for APT, figure 2.6 (c). During milling, the Pt cap gradually erodes providing the user the opportunity to shape the sample's shank into the needle shape. The latter milling steps are performed at lower beam currents, such as 0.3 nA, to reduce the speed of cutting and allow the user to control the milling rate. A 5 keV mill, accomplished by simply imaging the sample, is done to reduce the ion damage and implantation on the surface by milling it away.

2.6.2 Atom probe data analysis

Once an atom probe data set is collected, it was analyzed by the following:

Basic atom map visualization:

The collected atoms are reconstructed and viewed using the Imago Scientific IVAS 3.4.1 platform. Visualization of the samples is done by making atom maps of the reconstructed volumes. From these volumes, different atoms within the microstructure can be viewed by selecting and deselecting them in the viewing window, creating isoconcentration surfaces and/or 2D concentration maps, all of which can assist in characterizing the material.

Compositional profiles and proximity histograms (proxigrams):

A 2D concentration profile was created to depict elemental concentrations within the films. This profile creates a planar image that displays ‘hot spots’ of highly concentrated areas of a specified element within a data set. These images are analogous to contour maps.

A proximity histogram (proxigram) is used to measure the concentration difference between an interfacial surface and the matrix.²⁶ The proxigram outputs data identical to that of a normal concentration profile except the proxigram takes into account interface roughness and contour changes. An isoconcentration or isodensity surface is constructed and the concentration, as a function of distance from that surface, is calculated. The distance is measured as the proximity of each point of space to the reference surface.^{19,21,26}

Positive and negative proximities correspond to the point of space being on different sides of the surface. This provides a clear means of identifying the concentration profile from a defined interface, such as a grain boundary.

Clustering analysis:

In this experimental analysis, clusters were defined as a collection of atoms where the concentration of Ta is greater in a particular area as compared to that of the matrix. These ‘clusters’ which can be diffuse or concentrated spatially consisted of Fe, Pt, and Ta atoms. The integrated cluster finding analysis tools in the IVAS 3.4.1 software was used to assist in obtaining cluster positional and compositional data. To verify the existence of clusters, a statistical methodology outlined by Moody *et.al.*²⁴⁻²⁵ was applied.

With this approach, voxels were constructed using blocks of 100 Fe-Pt atoms. The number of Ta atoms within each defined voxel is then plotted as a function of counts/frequency. This data was then compared to that of a random sample created from the experimental data. The deviation of the experimental data from that of a random distribution denotes solute segregation. As in Moody *et al.*'s²⁴⁻²⁵ analysis, a μ value, Appendix B, was calculated using the equations below.

$$\chi^2 = \sum_{n=0}^{n_b} \frac{(e(n) - f(n))^2}{f(n)} \quad (2.2)$$

$$\mu = \sqrt{\frac{\chi^2}{N + \chi^2}} \quad (2.3)$$

Where $e(n)$ is the number of blocks containing n solute atoms measured experimentally, $f(n)$ is the number of blocks containing n solute atoms measured randomly and N is the number of blocks sampled, equation 2.2-2.3.

This value measures the magnitude of random deviation, like that of χ^2 (used in significance testing)²⁵ but is independent of sample size.

CHAPTER 3

RESULTS & DISCUSSION

3.1 X-ray Diffraction

In the XRD scans, figure 3.1, the phase identification for the various films at different temperatures are shown. Upon annealing at 550°C the Fe₅₂Pt₄₈ film as well as the Fe_{52.3}Pt_{46.3}Ta_{1.4} ordered. This is evident by the characteristic (001) and (110) $L1_0$ reflections, as well as the clearly tetragonality splitting in the (200) and (002) peaks. This scan was taken at a chi of 35 °. The higher Ta content film (7.3 at. %) does not show any evidence of $L1_0$ ordered reflections at this time and temperature anneal; however at 750°C, all three compositions have ordered, figure 3.1(c). It appears that 1.3 at. % Ta does not significantly reduce the ordering behavior, in contradiction to Chen *et al.*'s.¹⁷ results for similar low Ta concentrations. Recall that Chen *et al.*¹⁷ reported that up to ~2 at. % Ta suppressed the order. The XRD results clearly showed that as the Ta content was increased, the ordering temperature increased.

The addition of Ta also resulted in a change in the fiber texture of the films. From the as-deposited XRD scan, figure 3.1(a), there is an inversion of the {111} and {200} fiber texture. In the binary film, the (111) dominates where as the ternary system the (200) dominates the growth direction. For face centered cubic (fcc) based structures, such as the A1 symmetry, the (111) closed packed planes is the lowest free energy surface.⁸ The formation of this surface competes with the lowest strain energy direction [100].⁸ The addition of Ta, even for the low amount of 1.3 at. %, allowed the strain energy direction to dominate the fiber growth of the film.

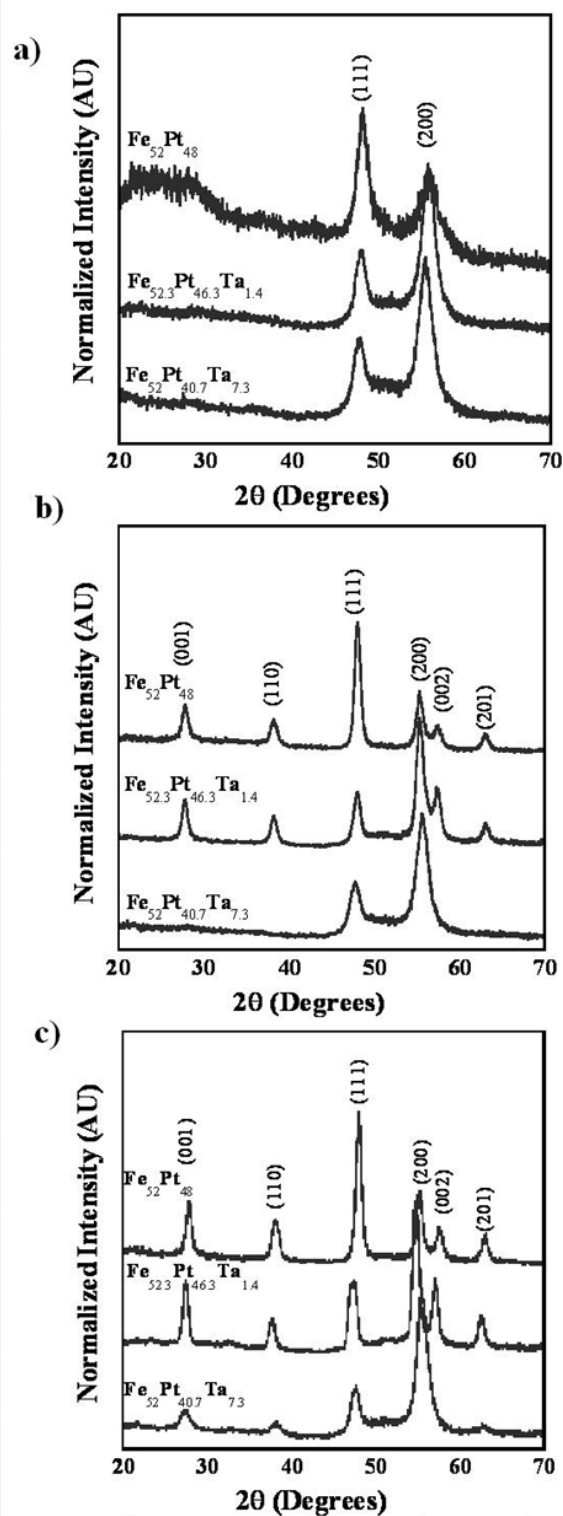


Figure 3.1 XRD scans of Fe₅₂Pt₄₈, Fe_{52.3}Pt_{46.3}(Ta_{1.4}) and Fe₅₂Pt_{40.7}(Ta_{7.3}) at the following conditions: (a) as-deposited (b) 550°C and (c) 750°C films.

Interestingly, the relative integrated intensity ratio of the (111)/(200) for both Ta concentrations was ≈ 0.5 suggesting small concentrations of Ta incorporation is sufficient to promote the low energy strain orientation as compared to the lowest free energy surface. The binary film's integrated (111)/(200) ratio was ≈ 1.7 . A slight shift to a lower d_{111} lattice spacing and higher d_{200} spacing can be seen between the binary and ternary films, consistent that a lattice strain was associated with the incorporation of Ta into the A1 phase. The incorporation of Ta, a larger atom than either Fe or Pt, clearly increases the driving force for the fiber texture change towards the favorable strain reduction direction.

The degree of order is plotted in figure 3.2. As evident from the XRD scans in figure 3.1, as Ta content is increased, the ordering was suppressed. Unlike Jin *et al.*¹⁵, the present work does not show that Ta promoted order. The order parameter for the 1.3 at. % Ta film is lower than that of the binary film. The 7.3 at. % Ta achieved an order parameter nearly one-half of that of the binary system at the highest annealing temperature of 750°C. These results clearly indicated that Ta suppressed ordering and confirmed the results of Chu *et al.*¹⁶

3.2 Magnetometry

Similar to the order parameter trends, the higher addition of Ta resulted in a drop in the H_c as a function of increasing Ta content, as plotted in figure 3.3(a). Interestingly, the 1.3 at. % Ta addition, though it had a slightly lower S , had nearly equivalent coercivity values for the temperatures studied. Other than the near zero H_c loops, those that exhibited significant hysteresis showed a hard and soft magnetic component, as plotted in figure 3.3(b) – (c). The presence of the soft component would suggest that a variation in the ordered fraction existed in the material, *i.e.* not all of the material phase transformed or achieved the same S value.

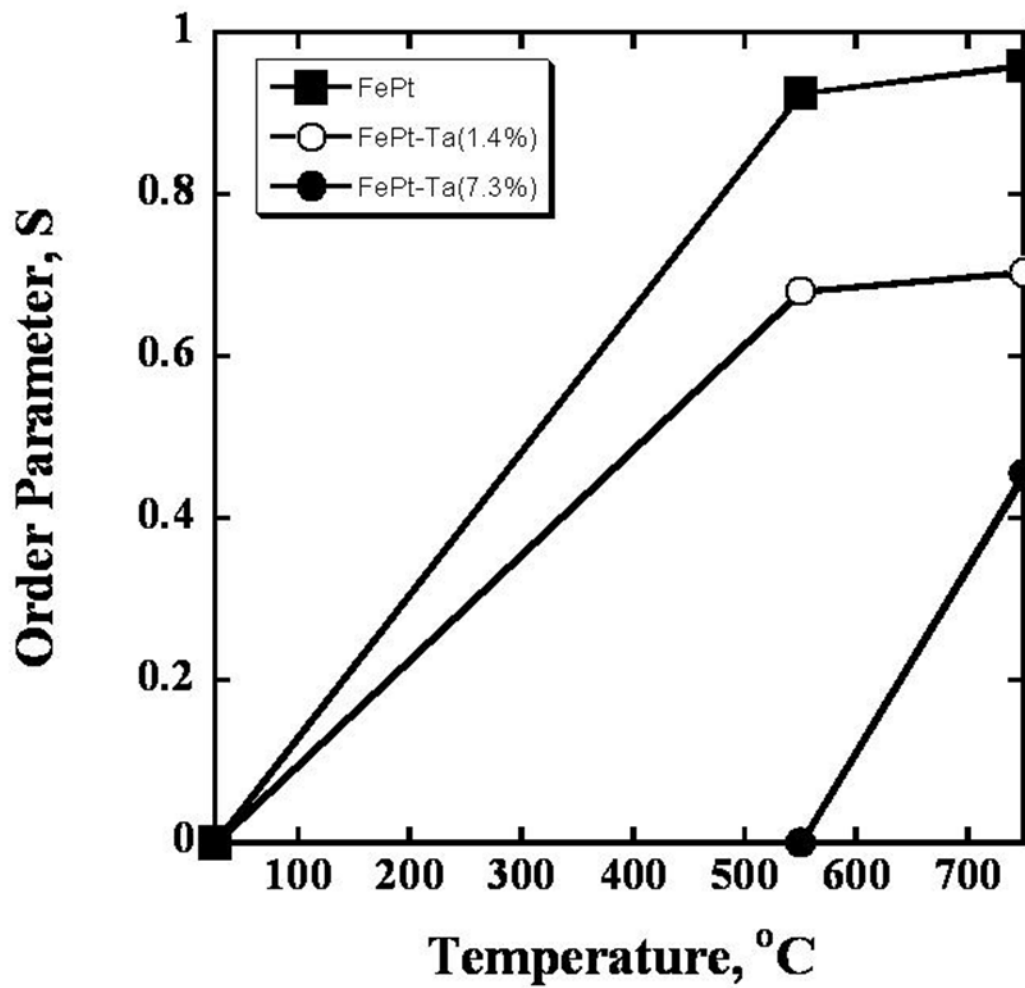


Figure 3.2 Order parameter values calculated using equation (2.1) .

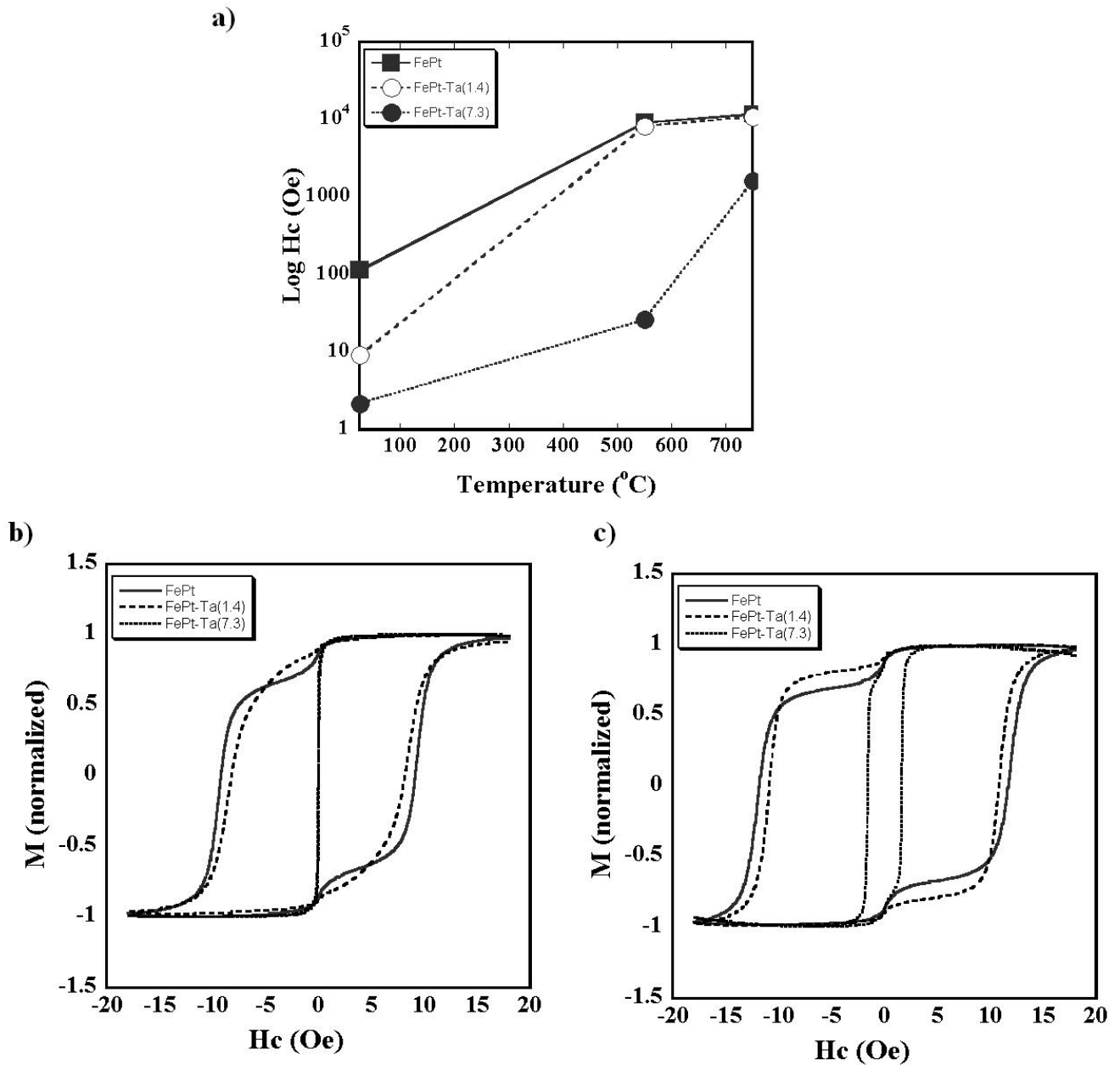


Figure 3.3 (a) Coercivity values obtained versus annealing temperature. AGM hysteresis loops with normalized magnetization values of (b) films annealed at 550°C and (c) films annealed at 750°C for 30 min.

3.3 Grain Growth

As the Ta concentration increased, the grain growth became more inhibited, as plotted in figure 3.4. This is in agreement with the other reports.¹⁵⁻¹⁷ The average grain size values given were taken from the mean values of the histograms. The histograms for each sample can be found in Appendix A. For the lower 1.3 at. % Ta concentration, only at the highest anneal was there significant deviation in grain growth between itself and the binary alloy. Interestingly, in the as-deposited condition, the grain size was larger than the binary alloy, figure 3.4, and could be because of the growth strains and promotion of this low strain energy texture.

3.4 Atom Probe Results

The atom probe results allowed for atomic identification and spatial location to address how Ta inhibited ordering and reduced grain growth. The as deposited $\text{Fe}_{52.3}\text{Pt}_{46.3}\text{Ta}_{1.4}$ film was analyzed and revealed that the Ta is indeed random in the A1 phase. This is verified statistically in figure 3.5. For the subsequent analysis, done via IVAS 3.4.1, the d_{max} and N_{min} values stayed constant for the samples with the same composition. The procedures are outlined in Appendix B. The maximum distance used in searching for neighboring solute ions is given by d_{max} and N_{min} is the minimum number of solute ions required in a cluster for it to be identified as a cluster. Keeping these values constant aided in the generation of consistent and comparable results.

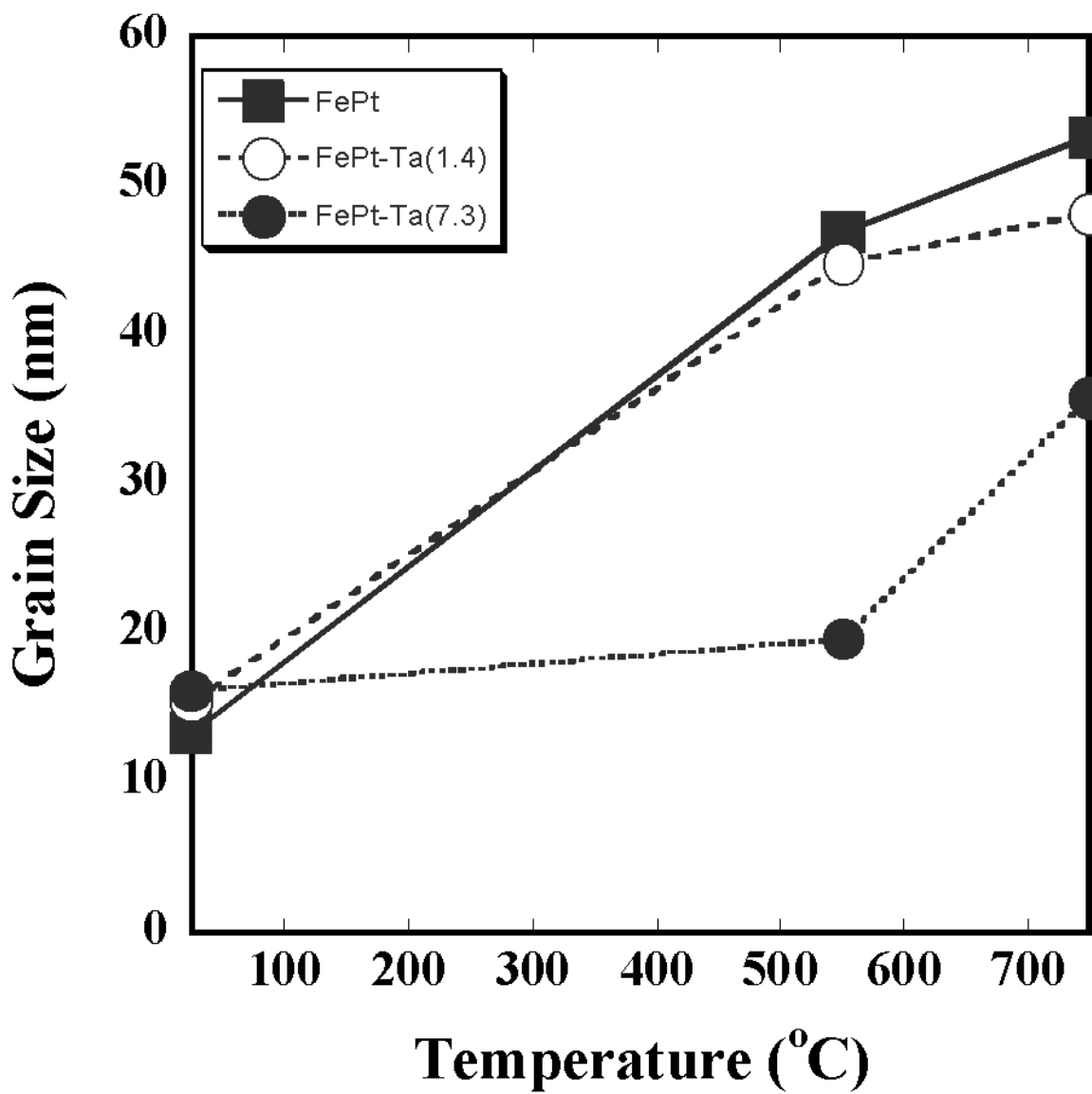


Figure 3.4 Average grain size values, taken from 50 grains, plotted versus annealing temperature.

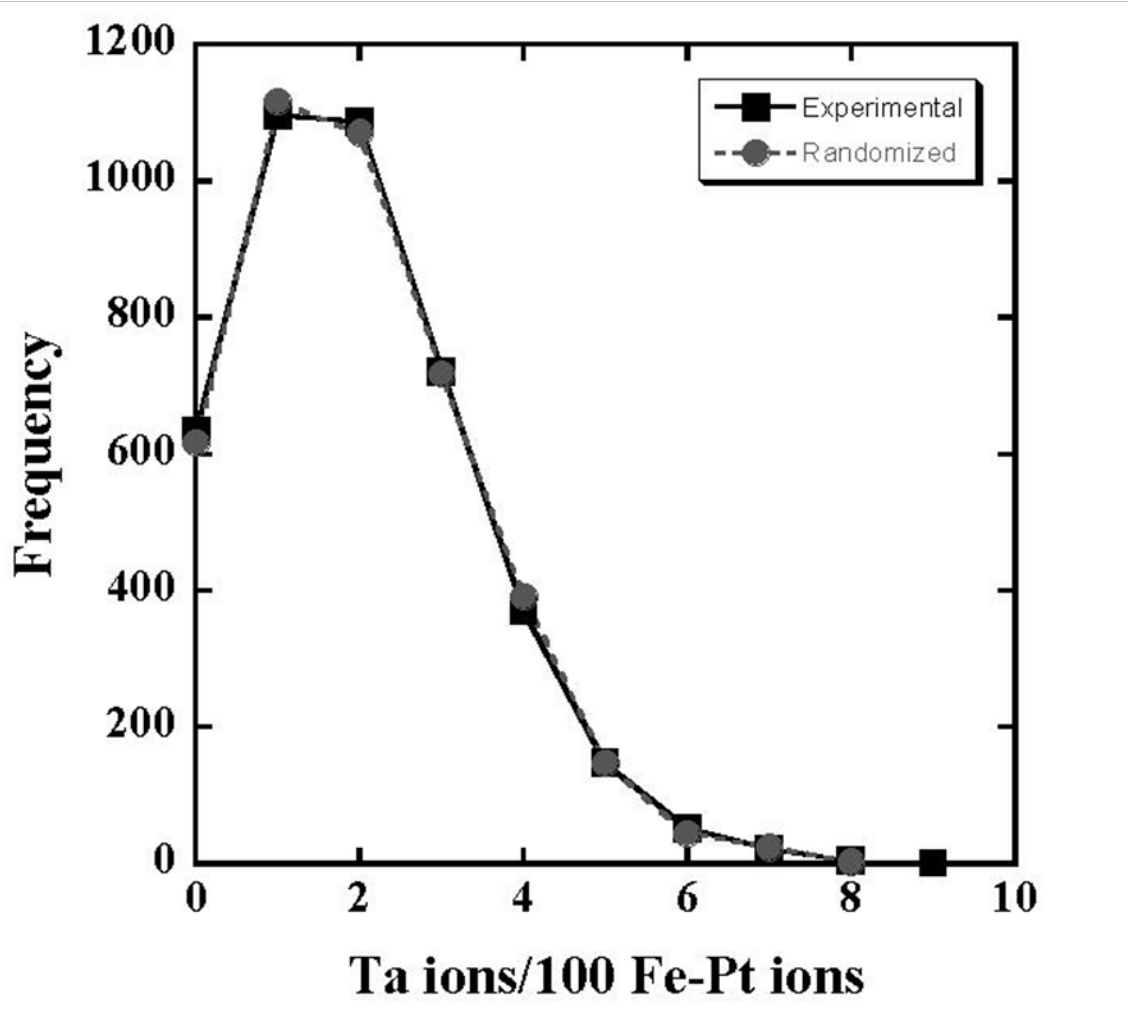


Figure 3.5 Statistical analyses for as-deposited $\text{Fe}_{52.3}\text{Pt}_{46.3}\text{Ta}_{1.4}$ film.

At 550°C, the $\text{Fe}_{52.3}\text{Pt}_{46.3}\text{Ta}_{1.4}$ film was ordered, as evident in the XRD spectrum of figure 3.1(b) and showed a small amount of clustering, via the plot in figure 3.6 (a). In this plot, a ‘random’ sample is overlaid with the experimental data. The experimental data showed a deviation from randomness which indicated that Ta has statistically clustered. Figure 3.6 (b) shows the statistical error in the plot of the random data versus experimental data. A 2D concentration profile, figure 3.6 (c), clearly indicates ‘hot spots’ of Ta within the matrix, but they do not appear to be localized. An atom map, figure 3.6 (d), indicated that the clusters appeared to have formed within the grain. The atom map was that of Si, which was an intrinsic impurity from the Fe target. The Si segregated to the grain boundaries providing ease in visual representation of the Ta-based clusters with respect to the microstructure. These clusters have a concentration that is slightly higher than that of the bulk, table 3.1. The average cluster composition was 51 at. % \pm 4.8, 42 at. % \pm 4.9 and 6 at. % \pm 1.8 for Fe, Pt and Ta respectfully with the balance being oxygen, silicon, hydrogen, etc. (intrinsic impurities from sputtering target). Clusters did not show enrichment of these impurities. Interestingly, the Ta is not migrating out of the grain to the boundaries but would rather form a new interface within the matrix. This local clustering into small ‘hot spots’ are allowing regions of nominal binary Fe-Pt to exist which may facilitate the distances where Ta does not inhibit short range order and the phase transformation can occur.

The $\text{Fe}_{52}\text{Pt}_{40.7}\text{Ta}_{7.3}$ film annealed at the same temperature and time (550 °C/30 minutes) does not show XRD evidence of $L1_0$ ordering in figure 3.1(b). Interestingly, the statistical cluster analysis plots in figure 3.7 (a) showed a greater deviation between the random sampling and experimental data which indicated clustering. The 2D concentration plots showed local ‘hot spots,’ similar to figure 3.7 (b), but the overall Ta concentration between the ‘hot spots’ was much higher and uniform throughout the microstructure.

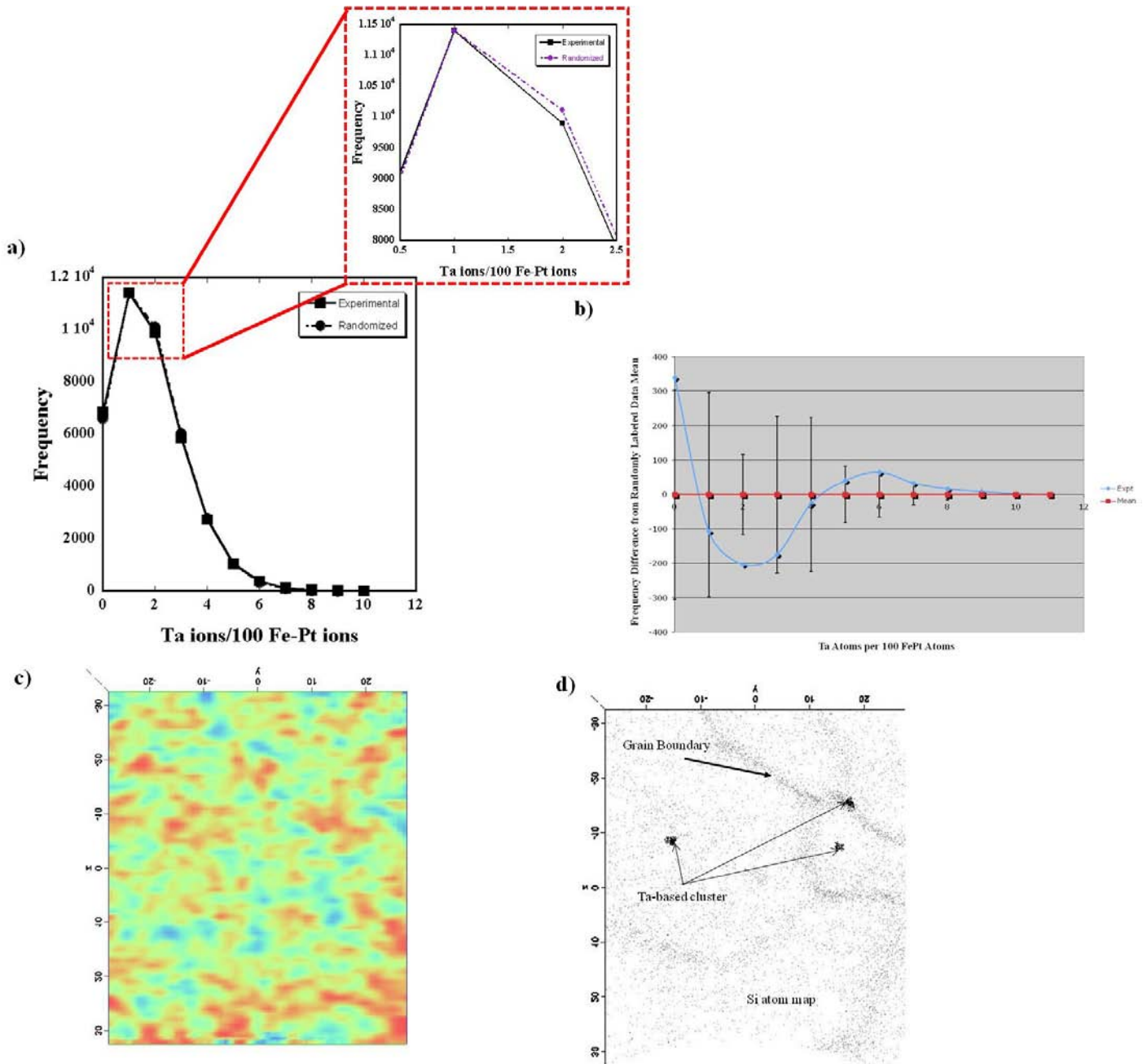


Figure 3.6 (a) Statistical analyses, (b) comparison of experimental data with mean random standard deviation (c) 2D concentration map and (d) atom map of Si for 1.4 at% Ta film annealed at 550 °C.

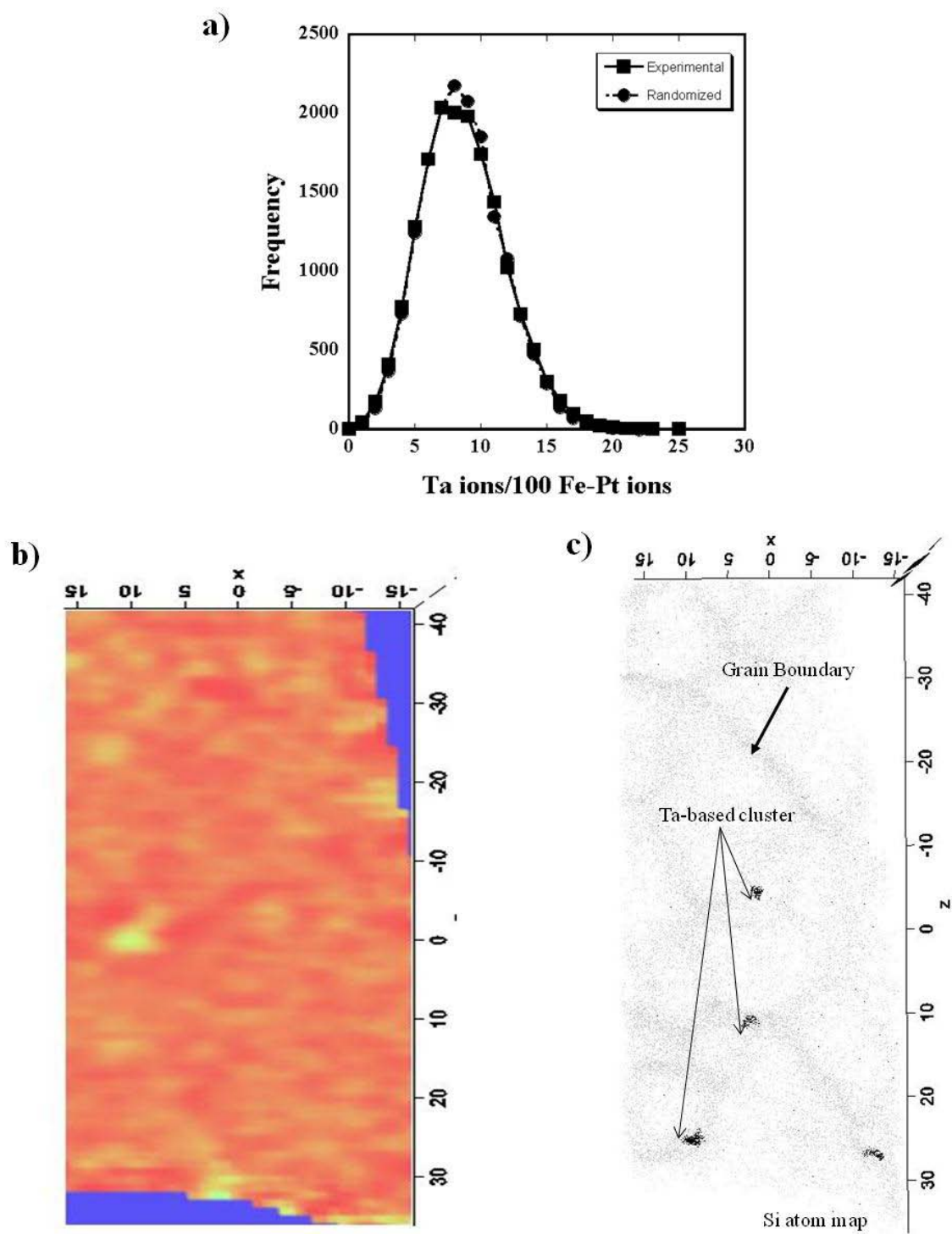


Figure 3.7 (a) Statistical analyses, (b) 2D concentration map and (c) atom map of Si for 7.3 at% Ta film annealed at 550 °C.

Table 3.1 Composition of clusters in Fe_{52.3}Pt_{46.3}(Ta_{1.4}) annealed at 550°C

	Solute Ions	Atomic % Pt	Atomic % Ta	Atomic % Fe
Cluster 1	9	44.81	5.84	48.70
Cluster 2	9	37.21	4.19	54.88
Cluster 3	9	31.38	4.79	59.04
Cluster 4	8	36.92	6.15	53.85
Cluster 5	16	35.82	4.12	55.93
Cluster 6	8	40.51	5.06	53.80
Cluster 7	8	47.78	8.89	43.33
Cluster 8	8	42.17	9.64	45.78
Cluster 9	8	44.63	6.61	48.76
Cluster 10	11	43.75	4.58	48.33
Cluster 11	10	43.86	5.85	47.95

Table 3.2 Composition of clusters in Fe₅₂Pt_{40.7}(Ta_{7.3}) annealed at 550°C .

	Solute Ions	Atomic % Pt	Atomic % Ta	Atomic % Fe
Cluster 1	21	39.84	16.41	42.97
Cluster 2	20	37.23	14.60	43.80
Cluster 3	23	37.06	13.53	44.71
Cluster 4	21	38.36	14.38	43.84

The high melting temperature of Ta, which is indicative of a slow diffusing species, suggested that it is more difficult at high concentration to be rejected from the FePt matrix. The higher concentration of Ta within the matrix is likely inhibiting the Fe-Pt short range ordering, unlike the lower concentration species in figure 3.6(b). An atom map of these clusters revealed their presence within the grain boundaries. At these higher concentrations of Ta, either diffusion is limited within the matrix for local clustering and/or clustering becomes more favorable in the grain boundaries. Cluster formation in the grain boundaries would not require the same energy penalties as forming in a matrix because the grain boundaries already have an interfacial energy contribution. The composition and number of atoms per cluster are tabulated in table 3.2. The average composition of the cluster was 44 at. % \pm 0.7, 38 at. % \pm 1.3 and 14 at. % \pm 1.2 for Fe, Pt and Ta respectively with the balance being oxygen, silicon, hydrogen, etc. (intrinsic impurities from sputtering target). Clusters did not show enrichment of these impurities.

The proxigrams for both the Fe_{52.3}Pt_{46.3}Ta_{1.4} and Fe₅₂Pt_{40.7}Ta_{7.3} samples are plotted in figure 3.8 through figure 3.11. The proxigrams were created by a density isosurface as the reference point. The isodensity surface was taken from the preferential segregation of Si into the boundaries, as noted previously. For the Fe_{52.3}Pt_{46.3}Ta_{1.4}, a slight decrease in the mean value of Ta concentration occurred as you approach the grain boundary, but this decrease is within the error bars of the analysis. This would suggest minimal depletion of Ta from the grains into the grain boundaries and would be consistent with the observation that clustering occurred within the grain itself. In contrast, the Fe₅₂Pt_{40.7}Ta_{7.3} film showed a significant depletion of Ta near the grain boundaries as compared to the bulk of the grain. As noted, Ta clusters were observed to be prevalent within the grain boundaries.

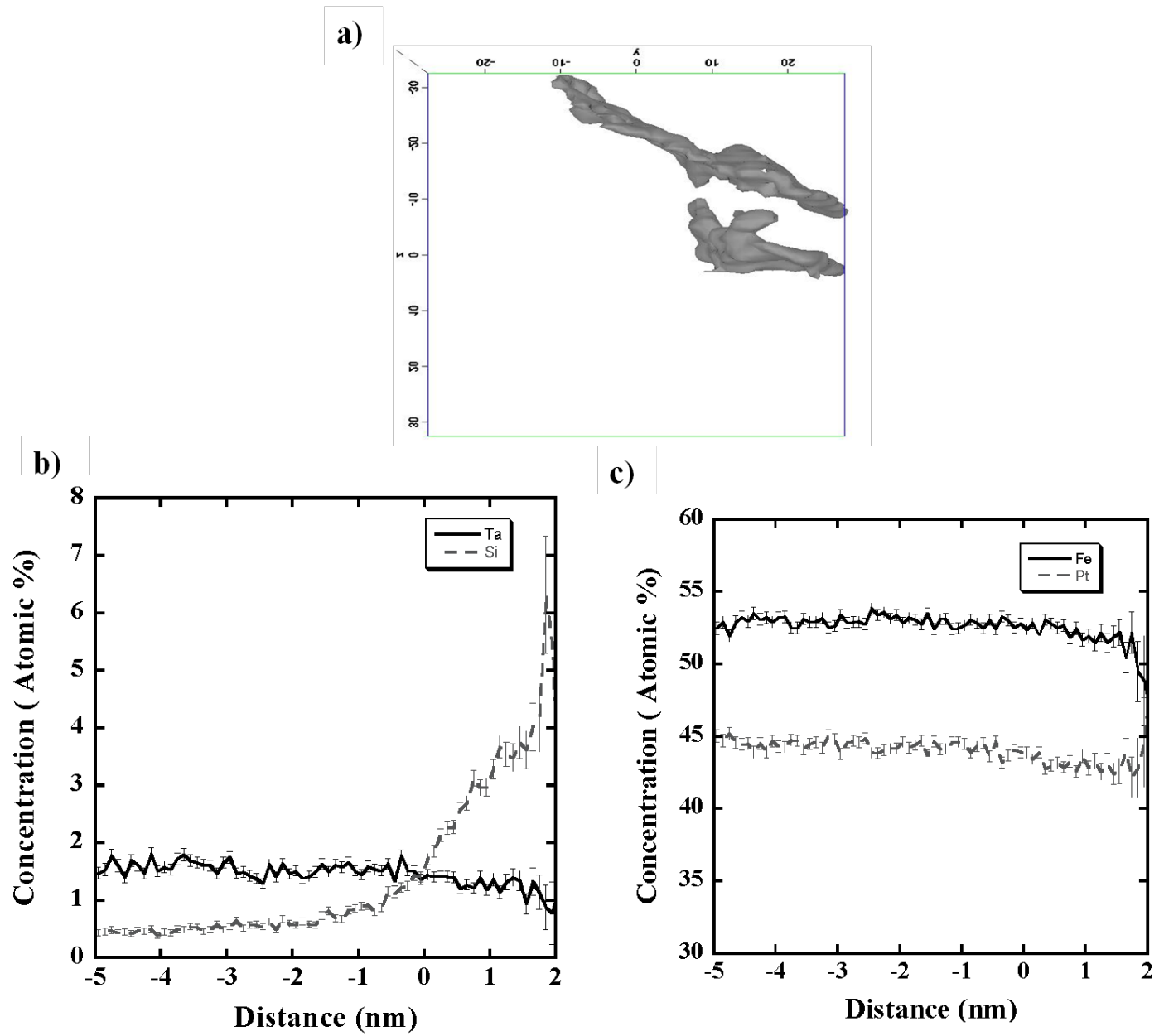


Figure 3.8 Proxigram from (a) isodensity surface of $\text{Fe}_{52.3}\text{Pt}_{46.3}\text{Ta}_{1.4}$ sample annealed at 550°C (b) concentration gradient of Ta and Si and (c) concentration gradient of Fe and Pt.

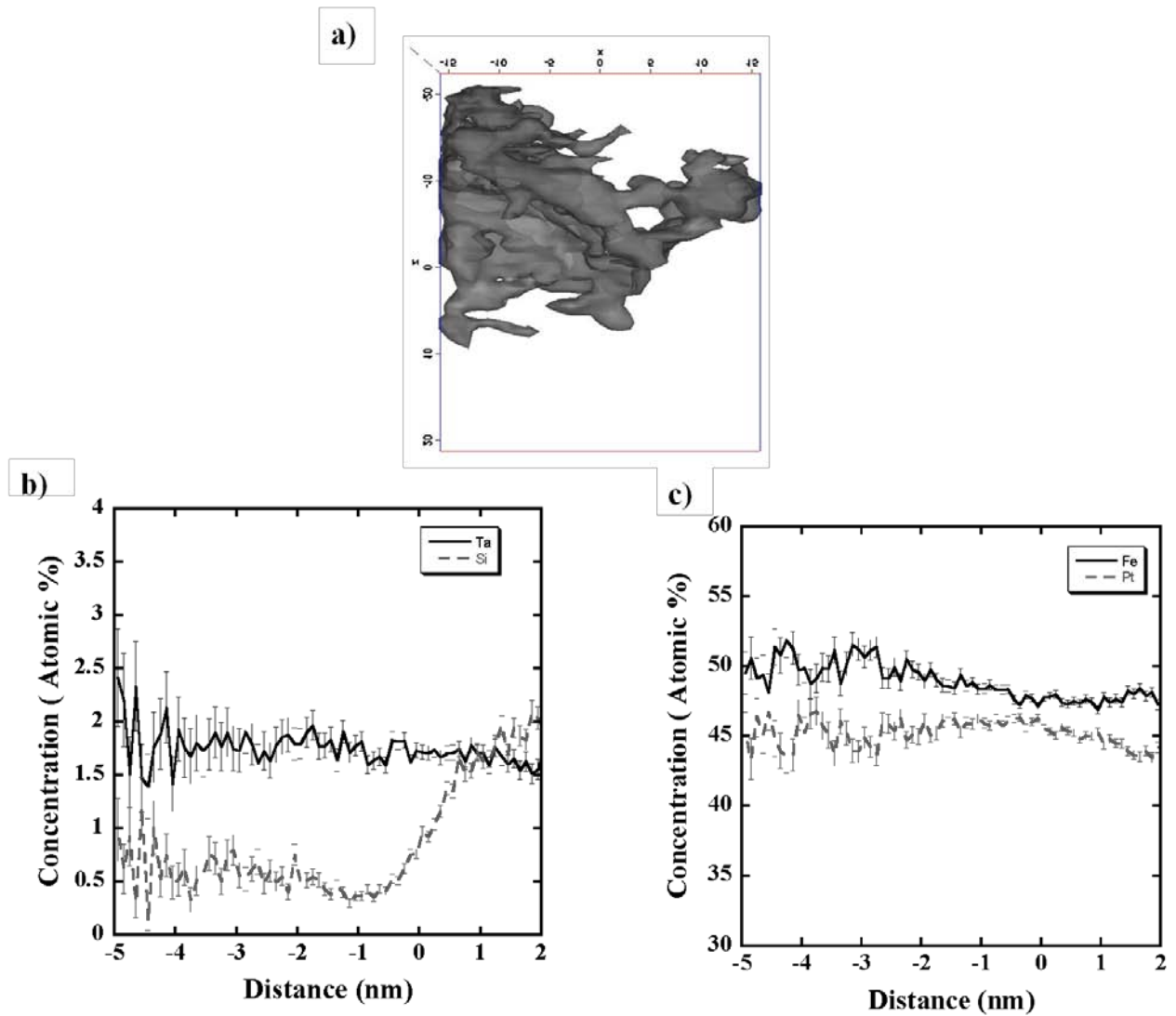


Figure 3.9 Proxigram from (a) isodensity surface of $\text{Fe}_{52.3}\text{Pt}_{46.3}\text{Ta}_{1.4}$ sample annealed at 750°C , (b) concentration gradient of Ta and Si and (c) concentration gradient of Fe and Pt.

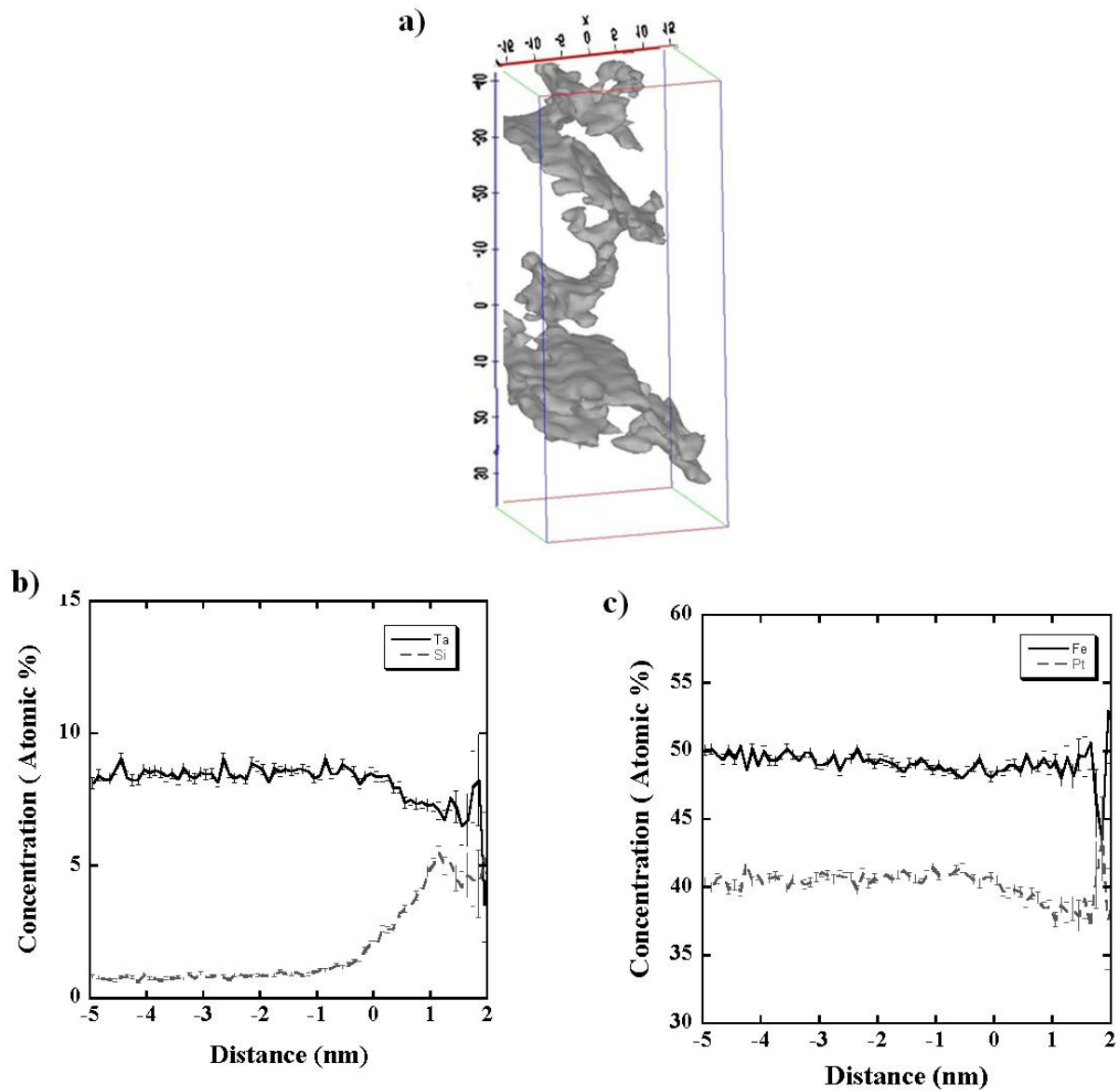


Figure 3.10 Proxigram from (a) isodensity surface of from $\text{Fe}_{52}\text{Pt}_{40.7}\text{Ta}_{7.3}$ sample annealed at 550°C , (b) concentration gradient of Ta and Si and (c) concentration gradient of Fe and Pt.

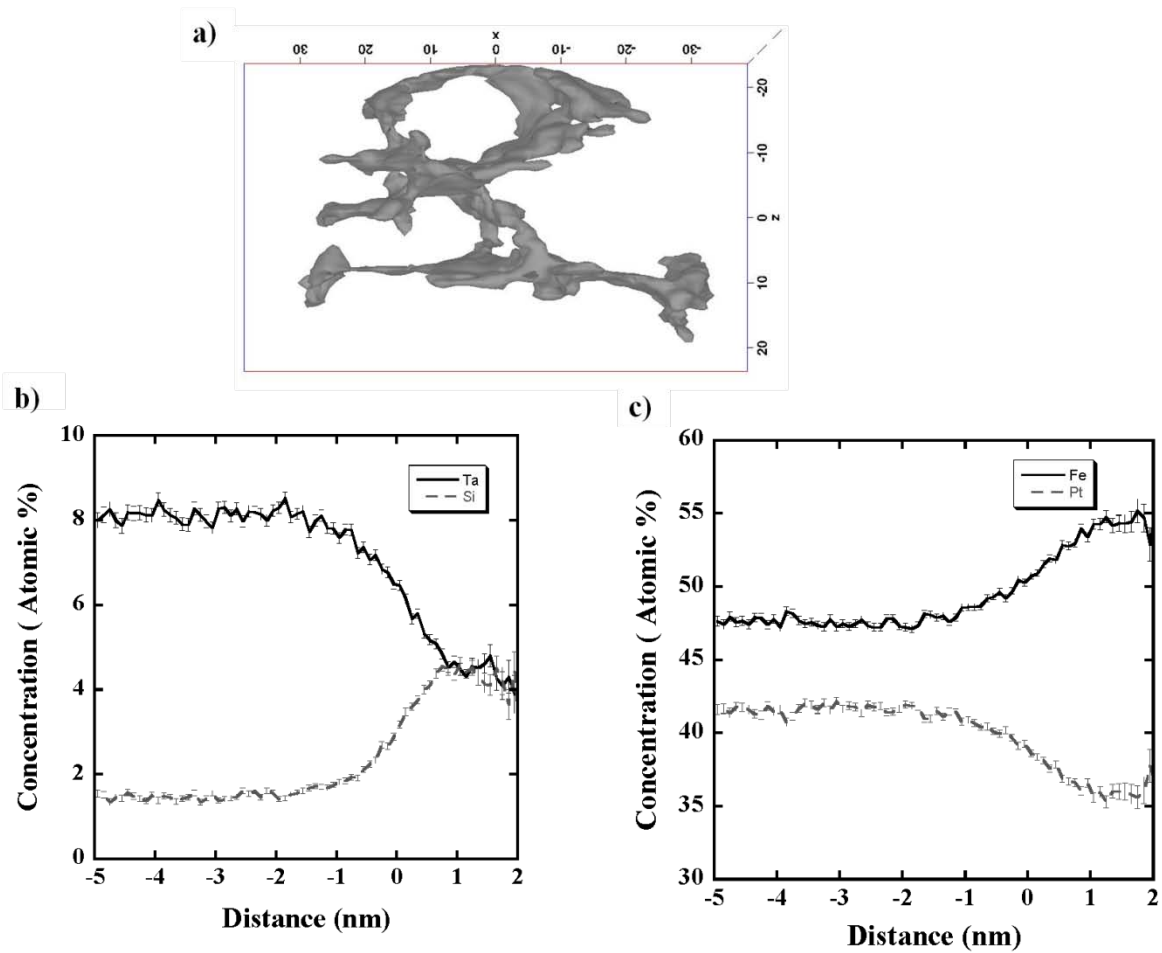


Figure 3.11 Proxigram from (a) isodensity surface of $\text{Fe}_{52}\text{Pt}_{40.7}\text{Ta}_{7.3}$ sample annealed at 750°C , (b) concentration gradient of Ta and Si and (c) the concentration gradient of Fe and Pt.

This decrease in Ta near the grain boundaries would be indicative of Ta being extracted from the grain (source for Ta) into the grain boundaries where upon it clustered. This would be analogous to solute depletion near precipitate free zones.²⁶ For both films, the grain boundaries were enriched in Fe as seen in the proxigrams.

Upon annealing the film to 750°C for 30 minutes, the $\text{Fe}_{52.3}\text{Pt}_{46.3}\text{Ta}_{1.4}$ continued to show clustering, as evident by the greater deviation from randomness in figure 3.12 (a). A comparison of the 2D concentration maps between figure 3.12(b) and figure 3.9(c) clearly shows a continual depletion of Ta within the matrix of the film. Atom maps, figure 3.12(c), also revealed a distribution of cluster sizes, but in general, it appears the clusters are coarsening. The smaller clusters are believed to be new clusters that have formed at this annealing condition. At this higher annealing temperature, the presence of clusters at the grain boundaries is noted in the atom map. The composition and number of atoms per cluster are tabulated in table 3.3. The average composition is 49 at. % \pm 1.1, 40 at. % \pm 1.2 and 6.2 at. % \pm 1.7 for Fe, Pt and Ta respectively with the balance being oxygen, silicon, hydrogen, etc. (intrinsic impurities from sputtering target). Clusters did not show enrichment of these impurities.

For the $\text{Fe}_{52}\text{Pt}_{40.7}\text{Ta}_{7.3}$ film annealed at 750°C for 30 minutes, the film did show evidence for $L1_0$ ordering, figure 3.1(c). Similarly to the $\text{Fe}_{52.3}\text{Pt}_{46.3}\text{Ta}_{1.4}$ film, there is a greater deviation from randomness, figure 3.13(a), and clustering is becoming more pronounced. The 2D composition map showed a clear depletion of Ta within the matrix, which would indicate that, the removal of the Ta from which short range FePt $L1_0$ ordering could occur. Clustering is prevalent in the grain boundaries and appeared to be coarsening, as evident in the atom map of figure 3.13(c). The clusters are also forming at the nodes of the grain boundaries. The proxigram of figure 3.11 for this film does show a significant decrease in Ta near the grain boundaries.

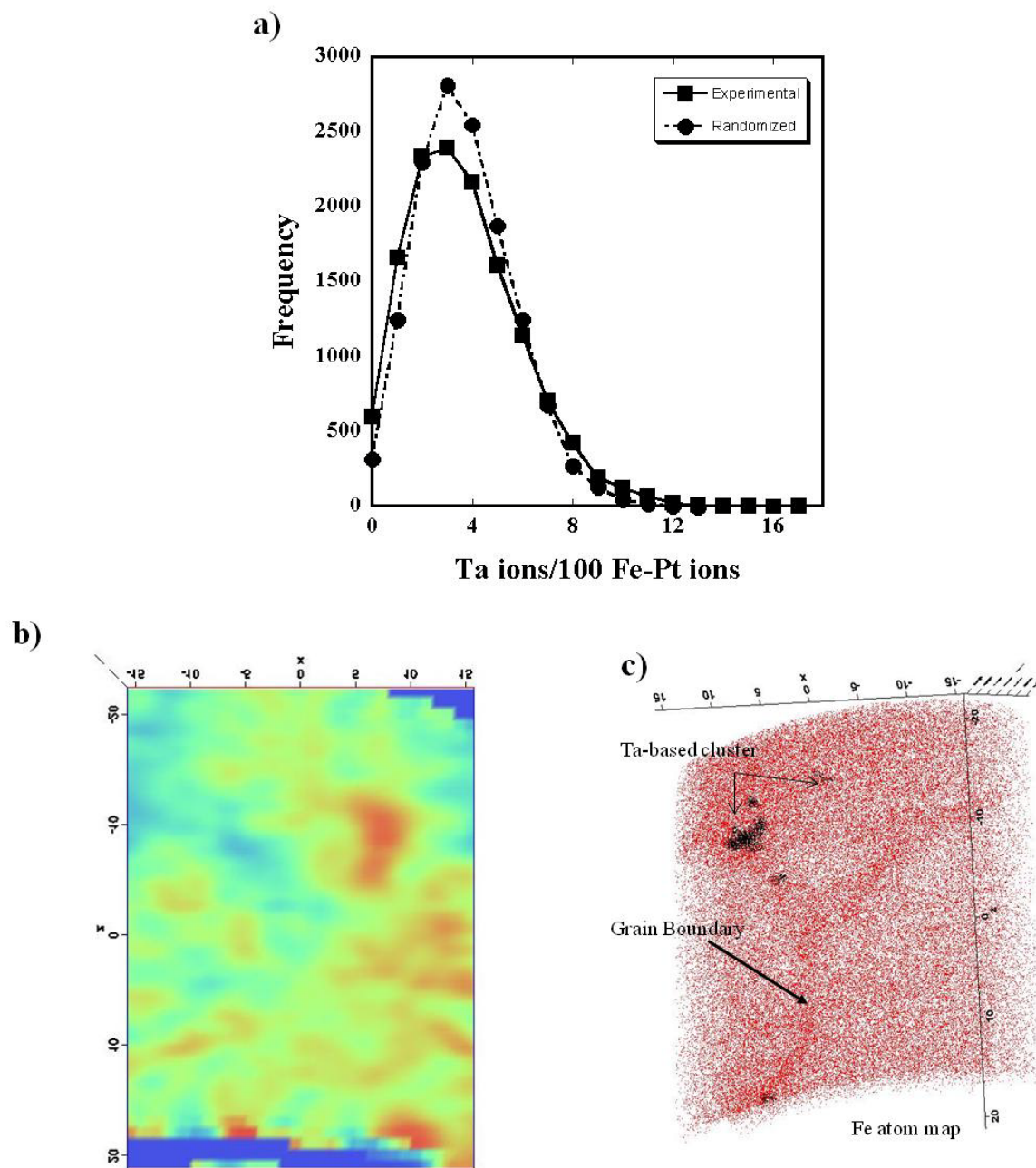


Figure 3.12 (a) Statistical analyses plot, (b) 2D concentration map and (c) Fe atom map for 1.4 at% Ta film annealed at 750 °C. The dark spots represent Ta-based clusters.

Table 3.3 Composition of clusters in Fe_{52.3}Pt_{46.3}(Ta_{1.4}) annealed at 750°C .

	Solute Ions	Atomic % Pt	Atomic % Ta	Atomic % Fe
Cluster 1	8	37.84	7.21	48.65
Cluster 2	8	39.04	5.48	51.37
Cluster 3	16	40.75	6.04	46.42
Cluster 4	15	39.59	7.61	47.72
Cluster 5	16	39.58	5.65	48.76
Cluster 6	16	38.85	5.76	50.36
Cluster 7	10	37.45	4.12	51.03
Cluster 8	9	38.52	7.38	48.36

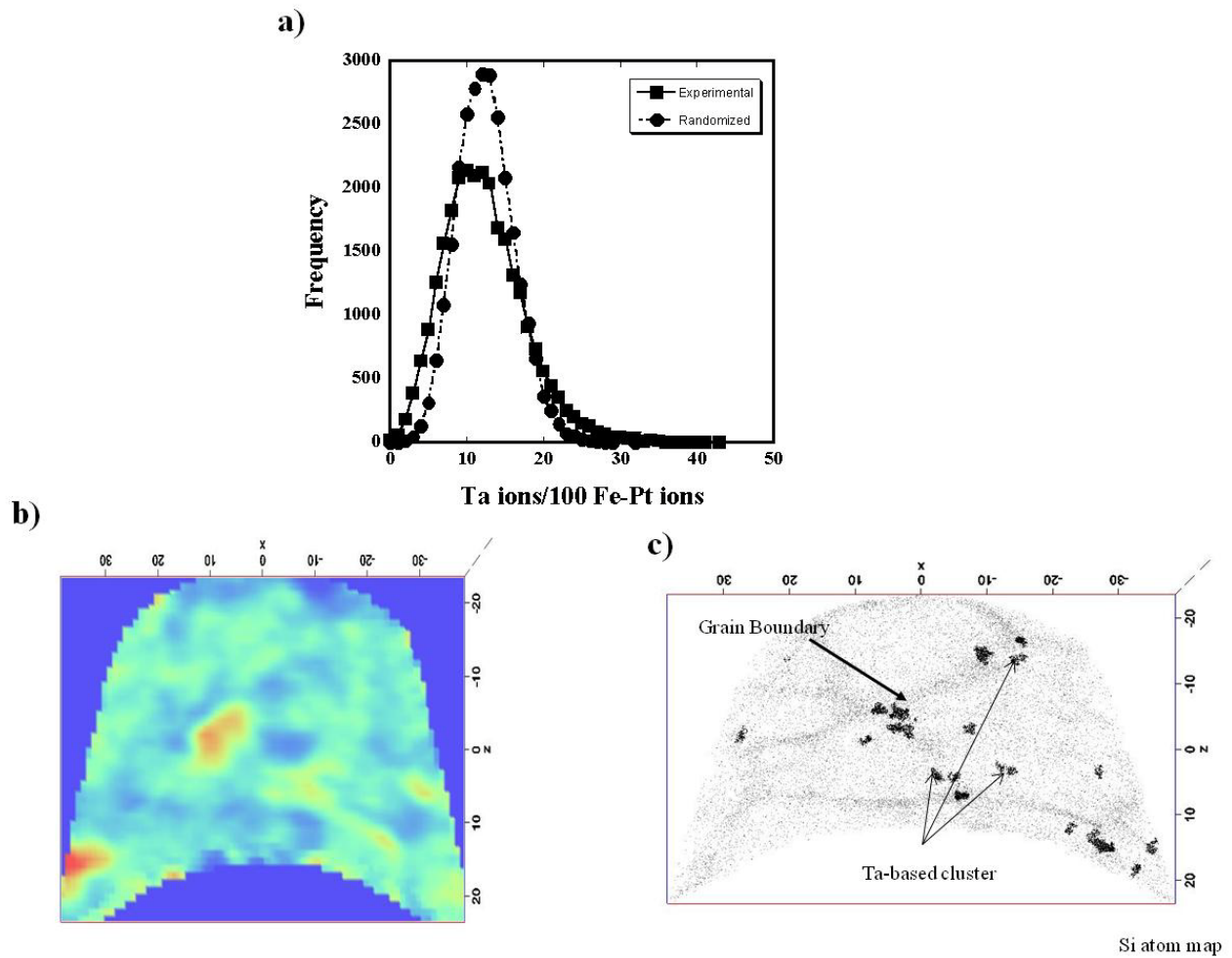


Figure 3.13 (a) Statistical analyses, (b) 2D concentration map and (c) Si atom map for 7.3 at% Ta film annealed at 750 °C. The dark spots represent Ta-based clusters.

This depletion of Ta out of the grain is the likely source of Ta for the coarsening clusters observed within the grain boundaries. Ta diffuses down the grain boundary and clusters together at these nodes. The composition and number of atoms per cluster are tabulated in table 3.4. The average compositions for the clusters are 41 at. % \pm 7.2, 41 at. % \pm 4.6 and 15 at. % \pm 4.9 for Fe, Pt and Ta respectively with the balance being oxygen, silicon, hydrogen, etc. (intrinsic impurities from sputtering target). Clusters did not show enrichment of these impurities.

The size, distribution and composition of the clusters depended upon the Ta addition and annealing treatment. At low temperatures and high concentrations, Ta inhibited the short range ordering of Fe-Pt necessary for the polymorphic A1 to $L1_0$ phase transformation. The clustering of Ta, from which Ta-free regions can form, is a necessary precursor step prior to ordering. The Ta clustering within the grain boundaries for the 7.3 at. % Ta film may help yield Ta-free Fe and Pt regions in and near the grain boundaries from which order can commence. Takahashi and Hono have suggested that ordering is a discontinuous precipitation event and will initiate at the grain boundaries. Li *et al.*²⁷ recently showed dark field TEM images which experimentally indicated the initiation of ordering at grain boundaries. The atom probe results clearly indicated that Ta, at relatively higher concentrations, inhibited ordering.

The propensity of clusters within the grain boundaries occurred as the Ta content increased. This grain boundary clustering aided in the grain refinement. These clusters could act as Zener pinning sites.²⁸ At 750°C, the $\text{Fe}_{52.3}\text{Pt}_{46.3}\text{Ta}_{1.4}$ film began to show deviation from the binary film in grain growth, figure 3.4. At this temperature clusters were observed in at the grain boundary, figure 3.12. At the lower anneal of 550°C the clusters were not at the grain boundary and the grain growth was similar to the binary film. For the $\text{Fe}_{52}\text{Pt}_{40.7}\text{Ta}_{7.3}$ the clusters were in the boundaries and limited grain growth occurred.

Table 3.4 Composition of clusters in Fe₅₂Pt_{40.7}(Ta_{7.3}) annealed at 750°C .

	Solute Ions	Atomic % Pt	Atomic % Ta	Atomic % Fe
Cluster 1	21	51.26	17.65	30.25
Cluster 2	23	40.65	14.84	43.23
Cluster 3	31	39.34	16.94	34.97
Cluster 4	23	41.81	12.99	40.68
Cluster 5	21	51.41	11.86	31.64
Cluster 6	24	38.17	18.32	41.22
Cluster 7	27	47.37	15.79	35.09
Cluster 8	21	36.36	8.68	51.24
Cluster 9	25	29.63	15.43	50.00
Cluster 10	48	38.51	10.50	47.48
Cluster 11	25	46.97	18.94	31.82
Cluster 12	22	37.14	6.98	51.43
Cluster 13	27	43.32	14.44	40.64
Cluster 14	22	37.29	7.26	51.49
Cluster 15	30	37.28	8.88	50.00
Cluster 16	25	42.78	13.89	40.56
Cluster 17	37	42.78	10.48	44.48
Cluster 18	39	42.28	9.26	41.57
Cluster 19	22	40.68	18.64	38.14
Cluster 20	23	32.71	21.50	42.99
Cluster 21	25	41.57	28.09	26.97
Cluster 22	21	45.16	22.58	27.96
Cluster 23	25	44.25	14.37	37.93
Cluster 24	30	42.86	17.14	34.86
Cluster 25	27	40.40	17.88	37.75
Cluster 26	24	42.41	15.19	38.61
Cluster 27	28	48.72	23.93	25.64
Cluster 28	20	44.44	9.66	44.93
Cluster 29	20	41.32	16.53	41.32
Cluster 30	20	37.98	15.50	44.19
Cluster 31	28	41.92	16.77	37.13
Cluster 32	25	45.54	22.32	30.36
Cluster 33	23	36.72	17.97	42.97
Cluster 34	22	31.14	13.17	50.90
Cluster 35	20	42.45	18.87	36.79
Cluster 36	42	40.09	18.50	38.77
Cluster 37	21	36.43	15.00	40.71
Cluster 38	51	40.36	15.13	41.25
Cluster 39	32	35.19	11.85	48.15
Cluster 40	27	44.00	21.60	34.40
Cluster 41	29	41.51	13.68	41.51
Cluster 42	20	38.36	4.57	51.83
Cluster 43	27	42.11	17.76	38.82
Cluster 44	25	42.94	14.12	37.29
Cluster 45	21	34.52	8.33	54.76
Cluster 46	25	33.98	24.27	40.78
Cluster 47	20	41.67	18.52	33.33
Cluster 48	20	36.24	13.42	49.66
Cluster 49	35	38.83	12.03	46.39
Cluster 50	21	41.30	15.22	39.13
Cluster 51	20	34.76	12.20	51.22
Cluster 52	23	39.67	7.54	49.18

The obvious rejection of Ta from the ordered $L1_0$ grains to the grain boundaries will likely pin the boundary. The formation of Ta clusters in the grain boundaries is critical to refine and control the grain growth.

Though Jin *et al.*¹⁵, Chu *et al.*¹⁶ and Chen *et al.*¹⁷ suggested that elemental Ta inhibited grain growth, this thesis provides first experimental evidence of the cluster chemistry (which is not elemental Ta), and its presence and distribution within the grain boundaries.

CHAPTER 4

CONCLUSIONS AND FUTURE WORK

This thesis differed from other studies done on FePt-Ta because it provided direct microstructural characterization, at the atomic level, to fully rationalize how Ta affected the ordering transformation or inhibited the grain growth. The collective results of the two annealing treatments for the two different Ta concentrations studies have brought about the following conclusions:

1. A critical level of Ta clustering (or absence within the grain) is required to allow the A1 to $L1_0$ ordering reaction in FePt to proceed. Clearly the presence of Ta to hindered the initial short range $L1_0$ ordering of FePt.
2. For low concentrations of Ta, clustering within the interior of the grain occurred. In contrast, the higher concentration of Ta did not show this type of clustering. For these higher concentration Ta films, a depletion of Ta near the grain boundaries was observed. This resulted in the direct clustering of Ta within the grain boundaries and refined the grain size and reduced the growth. The inhibited growth maybe because of a Zener pinning mechanism.²⁸
3. By removing the Ta near the grain boundaries for the higher concentration Ta film, nominal binary Fe-Pt composition would exist. The ordering reaction is suspected to be a discontinuous precipitation process that initiates at or near the grain boundaries^{7,12} and the reaction front then proceeds through the grain. This

4. Ta depletion zone may assist in this process. Even though Ta depletion was noted in the proxigram of figure 3.7(b) at 550 °C for the 7.3 at.% Ta film, the 2D map for this temperature clearly showed a high level of Ta throughout the grain which prevented ordering. Not until 750 °C was the depletion of Ta within the grains significantly reduced and ordering commenced.
5. For the lower concentration species of Ta, the clustering and significant reduction of uniform Ta within the grain was observed and order could be achieved at 550°C. Higher annealing temperatures of 750°C resulted in continued clustering and coarsening of the clusters. The clusters began to form at the grain boundaries and the grain growth was reduced as compared to the reference binary film.

In general, the discrepancies in reported results arise from the different deposition techniques and process settings used in the experiments.

The effect of the ternary addition of Ta to the FePt binary system was studied. However, there are further questions that have yet to be answered and are recommended for future work:

1. Introducing Ta into the FePt system resulted in change in fiber texture and an initial increase in the grain size. An investigation of how Ta controlled this change in texture and grain size would be interesting.
2. Attempts were done to image the clusters in the TEM but they were too small to get adequate diffraction contrast. Another study would be to clearly capture where grain boundary pinning by the clusters through an *in-situ* TEM experiment.
3. To better understand Ta clustering it may be beneficial to do a study that would determine the critical concentration where clusters form in the matrix versus those that formed in the grain boundaries at specific annealing temperatures. This would be added insight to microstructural engineering of the films.

REFERENCES

1. B. Zhang and W.A. Soffa, *Scripta Metallurgica* **3**, 683 (1994).
2. D. Weller, A. Moser, *IEEE Transactions on Magnetics*. **35**, 4423 (1999).
3. H.N. Bertram, H. Zhou, R. Gustafson, *IEEE Trans. Magn.* **34**, 1945 (1998).
4. S.H. Charap, P.L. Lu, Y. He, *IEEE Trans. Magn.* **33**, 978 (1997).
5. Platt, C. L., Wierman, K. W., Svedberg, E. B., Klemmer, T. J., Howard, J. K.,
Journal of Magnetism and Magnetic Materials, **247**, 2, 153-158 (2002).
6. M.F. Toney, W. Lee, J.A. Hedstrom and A. Kellock, *Journal of Applied Physics*
93, (2003).
7. Y.K.Takahashi, and K. Hono, *Scripta Materialia* **53**, 403(2005).
8. Ristau RA, Barmak K, Coffey KR, Howard JK. *J Mater Res* 14 (1999).
9. H. Okumura, S. Nishinakagawa, T. Bitoh, *Journal of Magnetism and Magnetic
Materials* **310**, 2527 (2007).
10. K.W.Wierman, C.L.Platt, and J.K.Howard, *J. Appl.Phys.* **93**, 7160 (2003).
11. C. Xiaomin, Y. Xiaofei, D Kaifeng, L. Zuoyi, *Journal of Wuhan University of
Technology-Materials Science Edition* **23**,5 (2008).
12. Y.K. Takahashi, M. Ohnuma, K. Hono, *Journal of Magnetism and Magnetic
Materials* **246**, 259 (2002).
13. S.R. Lee, S.Yang, and Y. K. Kim and J.G. Na, *Journal of Applied Physics* **91**, 10
(2002).

14. P. C. Kuo, Y. D. Yao, C. M. Kuo and H. C. Wu, *Journal of Applied Physics* **87**, 91 (2000).
15. S.Jin, S.U. Jang, and S. Kwon, Material Research Society Symposium Proceedings 998, (2007).
16. J. P. Chu, T. Mahalingam and S. F. Wang, *Journal of Physics: Condensed Matter* **16** 561–567 (2004).
17. G.J. Chen, Y.H. Chang, J.H. Lai, Y.L. Chai, *Journal of Magnetism and Magnetic Materials* **239**, 415–417 (2002).
18. JCPDS—International Center for Diffraction Data, Card No. 03-065-9121, (2005).
19. M. K. Miller *Surface and Interface Analysis* **31**, 593–598 (2001).
20. M.K. Miller, A. Cerezo, M.G. Hetherington, G.D.W. Smith, *Atom Probe Field Ion Microscopy*, Clarendon Press, Oxford, (1996).
21. M.K. Miller, M.G. Hetherington, *Surface Science* **246**, 332 (1991).
22. K. Thompson, D. Lawrence, D.J. Larson, J.D. Olson, T.F. Kelly, B. Gorman, *Ultramicroscopy* **107**, 131(2007).
23. K.L. Torres and G.B. Thompson, *Ultramicroscopy* **109**, 606 (2009).
24. M. P. Moody, L.T. Stephenson, P.V. Liddicoat, and S.P. Ringer *Microscopy Research and Technique* **70**, (2007) 258–268
25. Michael P. Moody,* Leigh T. Stephenson, Annav. Ceguerra, and Simon P. Ringer *Microscopy Research and Technique* **71**, 542–550(2008).
26. O. Hellman, J. Vandenbroucke, J. Blatz du Rivage, D. N. Seidman, “Application software for data analysis for three-dimensional atom probe microscopy,” *Materials Science and Engineering*, A327 29-33 (2002).

27. X.H.Li, B.T.Liu, W.Li, H.Y.Sun, D.Q.Wu, X.Y.Xhang, *Journal of Applied Physics* **101**,093911-1(2007).
28. D.A. Porter and K.E. Easterling, *Phase Transformations in Metals and Alloys* (2nd ed.) Chapman & Hall, London

APPENDIX A

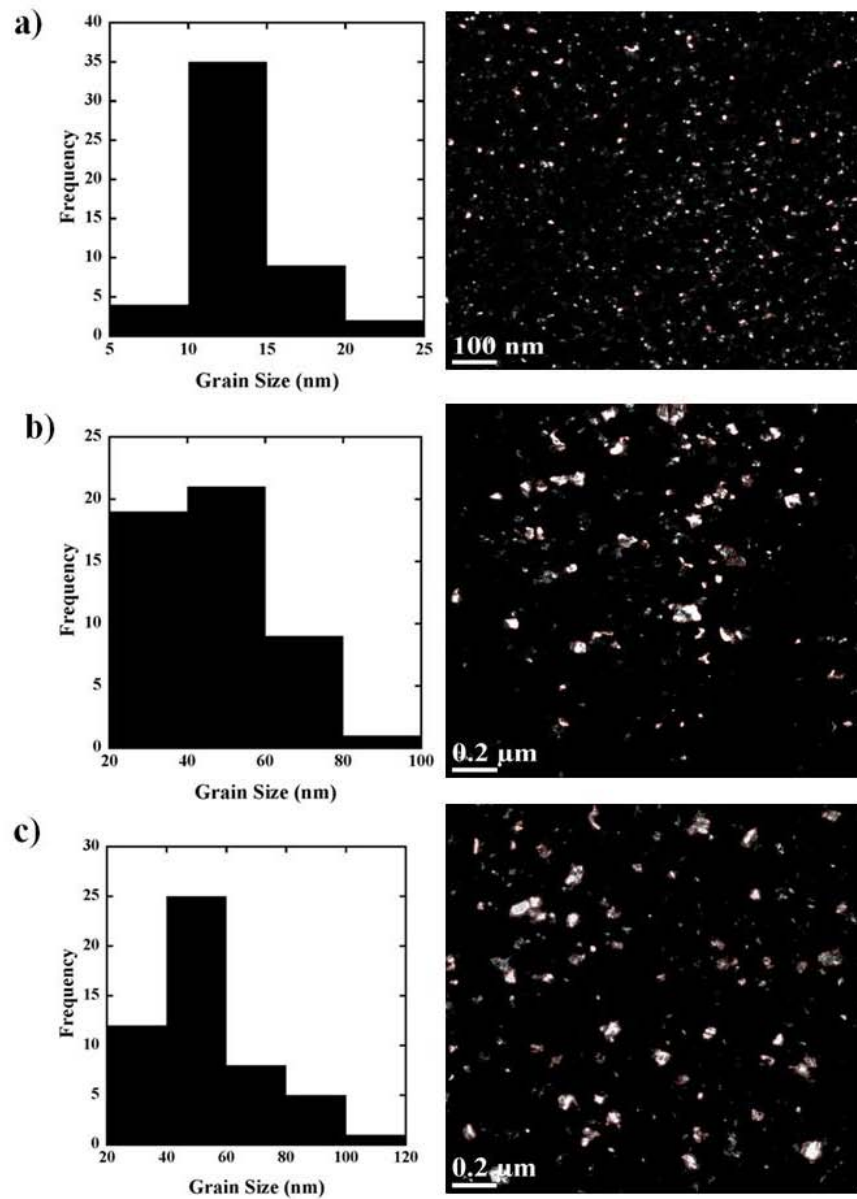


Figure A.1 Grain size distribution histogram with corresponding TEM micrographs for $\text{Fe}_{52}\text{Pt}_{48}$ film at the following conditions: (a) as-deposited, (b) 550°C and (c) 750°C .

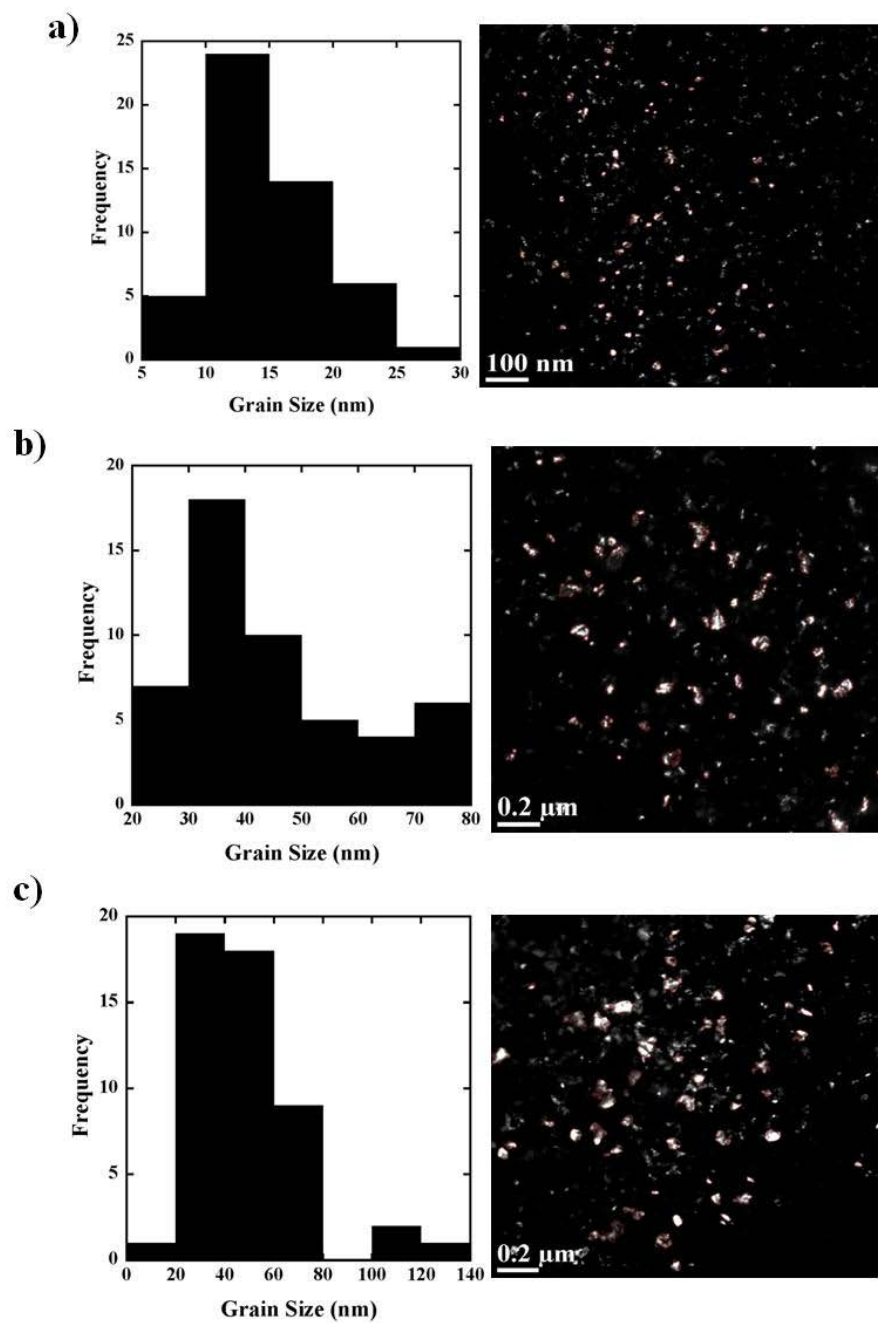


Figure A.2 Grain size distribution histogram with corresponding TEM micrographs for $\text{Fe}_{52.3}\text{Pt}_{46.3}\text{Ta}_{1.4}$ film at the following conditions: (a) as-deposited, (b) 550°C and (c) 750°C .

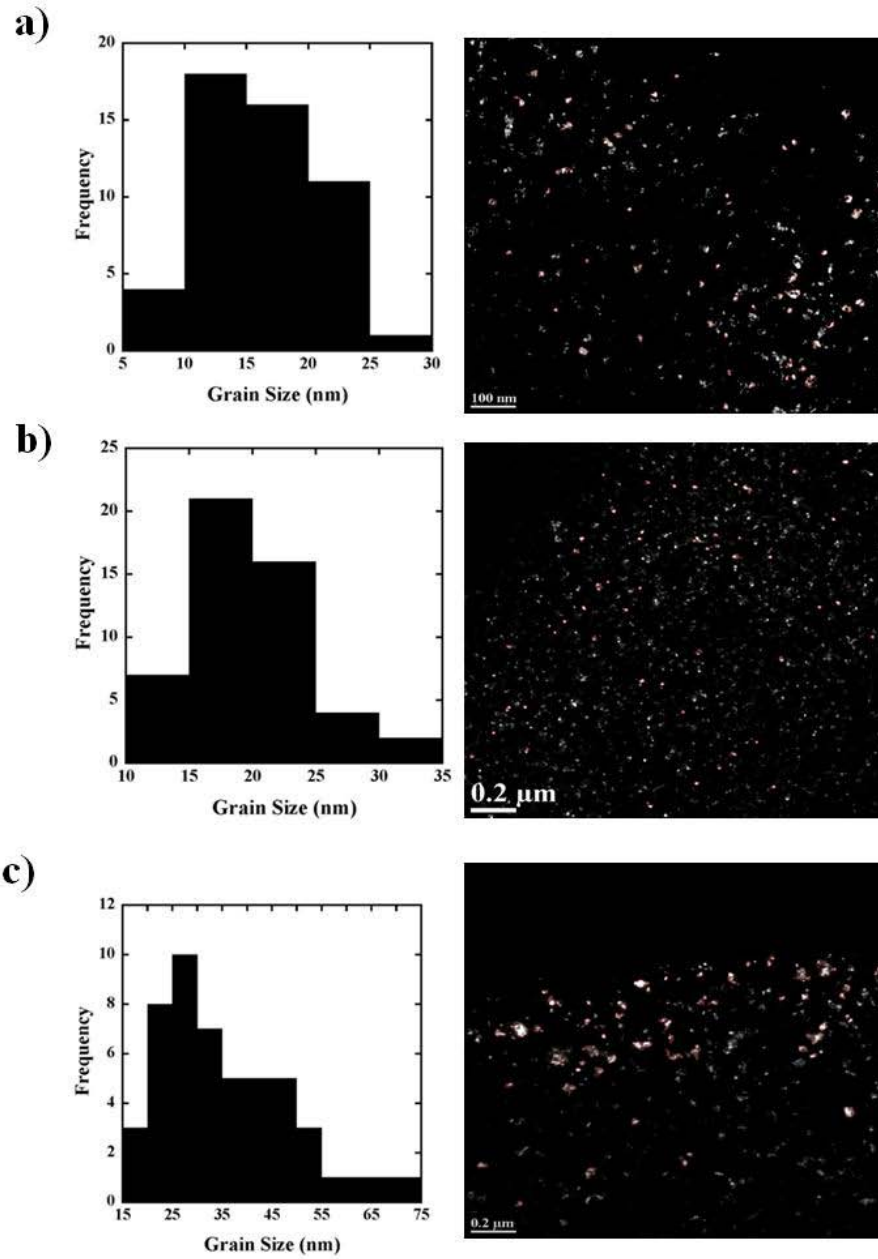


Figure A.3 Grain size distribution histogram with corresponding TEM micrographs for $\text{Fe}_{52}\text{Pt}_{40.7}\text{Ta}_{7.3}$ film at the following conditions: (a) as-deposited, (b) 550°C and (c) 750°C .

APPENDIX B

Table B.1 Mu (μ) values from statistical analysis.

	As Deposited	550°C	750°C
$\text{Fe}_{52.3}\text{Pt}_{46.3}\text{Ta}_{1.4}$	0.032	0.056	0.226
$\text{Fe}_{52}\text{Pt}_{40.7}\text{Ta}_{7.3}$	N/A	0.074	0.695

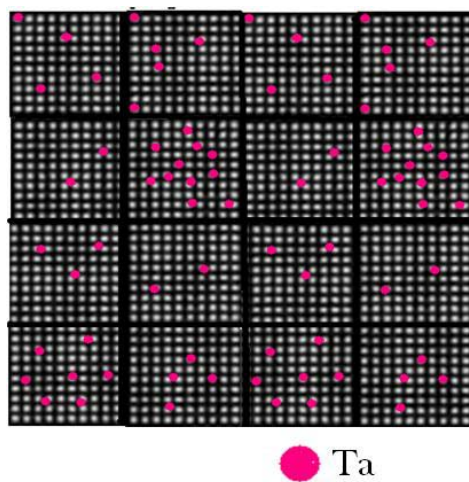


Figure B.1 Illustration of voxels.

Table B.2 IVAS 3.4.1 input parameters for identification of clusters.

	d_{\max} (nm)	N_{\min}
$\text{Fe}_{52.3}\text{Pt}_{46.3}\text{Ta}_{1.4}$	0.5	8
$\text{Fe}_{52}\text{Pt}_{40.7}\text{Ta}_{7.3}$	0.4	20

IVAS 3.4.1 Integrated Solute Analysis Techniques

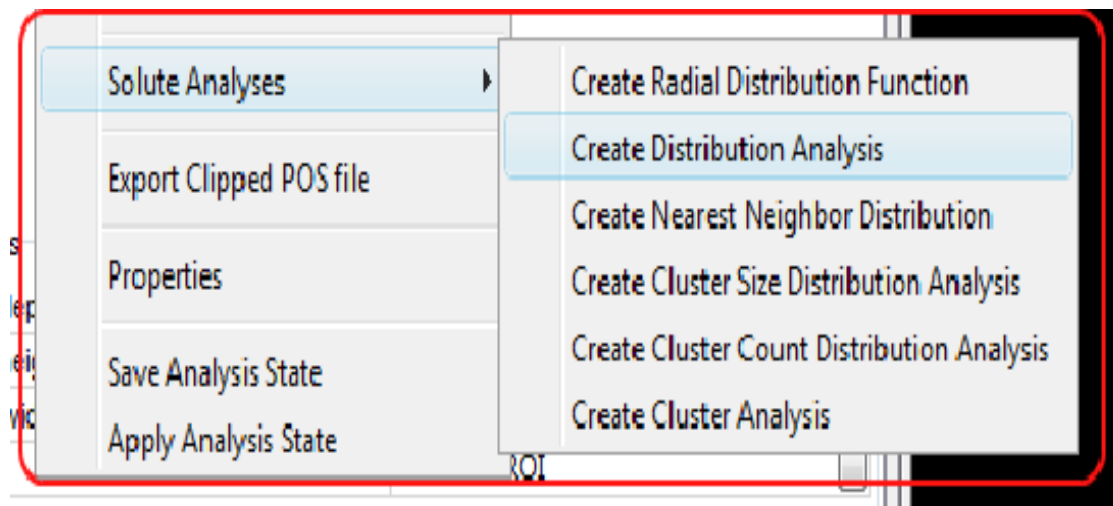


Figure B.2 IVAS solute analysis found by right clicking in analysis window.

Distribution Analysis

Before you get started on the cluster analysis it is important to check the data's randomness. This is done with the distribution analysis. NOTE: if the data is statistically random you should stop here.

- Step 1: Input sample counts (n).
 - This analysis collect n samples (ions) for the specified sample count, n, and computes the observed ion type concentration for the individual trial.

For solute concentrations lower than a few percent the number of counts may need to be increased, but in general a count size of 100 should suffice. Also, sample count may possibly need to be decreased if solute concentrations are higher than a few percent.

Step 2: Display

- The number of ions observed at a given concentration is shown as a stepped function (solid line).
- The theoretical binomial of homogenous data (randomized data) is displayed as a continuous function (dotted line).
- *Statistical analysis results numerically show the nonrandom specie, flagging nonrandom elements in red.*
- Note that both real clustered ions and matrix ions will be flagged as being nonrandom, but the matrix ions will be excluded from the cluster in a nonrandom manner).
- Regions where the two lines differ indicate clustering.

Nearest Neighbor Distribution

This analysis aids in determining a d_{\max} value. The plot generated calculates and compares pair-distance distribution data to randomized data. This helps to minimize the likelihood of several clusters being identified as one and statistically random clusters being counted as a cluster.

- Input
 - Maximum d_{pair} : Upper limit distance used to search for nearest neighbor.
 - Sample width d_{pair} : Scale of d_{\max} to be tested.
 - Order ions: 1 is used
- Output
 - Observed data (black plot) and random data (red plot).
 - d_{\max} should be taken between the two maxima.

Cluster Size Distribution

This analysis aids in searching for N_{\min} . For a given initial d_{\max} , a minimum cluster size that deviates from random can be found.

- Input
 - d_{\max} : Maximum distance used in searching for neighboring solute ions..
 - Order ions: 1 is used
- Output
 - The plot produced is that of observed data (black plot) and random data (red plot).
 - Cluster size limit, N_{\min} is found at or above the maximum of the random distribution data.

Create Cluster Count Analysis

This step fine-tunes the d_{\max} value. Enter the number you get for here and the plot generated will give you a number for d_{\max}

- Input
 - N_{\min} : least number of solute ions required in a cluster for it to be identified as a cluster. This value is taken from the cluster size distribution analysis.
- Output
 - The plot produced is that of observed data (black plot) and random data (red plot).
 - d_{\max} is found at the intersection of the two plots.

Create Cluster Size Distribution Analysis

Fine tunes N_{\min} so that the calculation for the final cluster analysis can continue without much interference from random clusters.

- Input
 - d_{\max} : Found in cluster count analysis..
- Output
 - The plot produced is that of observed data (black plot) and random data (red plot).
 - A final value for N_{\min} is determined.

Create Cluster Analysis

- Input
 - d_{\max} : Found in cluster count analysis..
 - Order (ions) - 1
 - N_{\min} – Least number of solute ions required in a cluster for it to be identified as a cluster. Found in second cluster size distribution run.
 - L (nm) - Envelope distance, constrained to $d_{\max}/2 \leq L \leq d_{\max}$, generally equal to d_{\max} .
 - d_{erosion} (nm) - Erosion distance. All clustered non-solute ions within d_{erosion} of any ion near that cluster are removed. Value is constrained to

$$0 \leq d_{\text{erosion}} \leq L.$$
- Output
 - A chart that contains cluster information, *i.e.* position, size statistics and cluster composition.
 - A visual representation of the clusters can be produced by exporting a *pos* file of the data and opened with the accompanied range file.